3B2v8.06a/w (Dec 5 2003).51c XML:ver:5.0.1 CSR : 1149 Prod.Type:FTP pp.1–28(col.fig.:4,5,8) ED:Nagesh PAGN:Uday SCAN:v4soft

ARTICLE IN PRESS

ELSEVIER

Available online at www.sciencedirect.com

SCIENCE DIRECT®

Continental Shelf Research ▮ (▮▮▮▮) ▮▮▮–▮▮▮

CONTINENTAL SHELF RESEARCH

www.elsevier.com/locate/csr

A cross-scale model for 3D baroclinic circulation in estuary–plume–shelf systems: I. Formulation and skill assessment

Yinglong Zhang, António M. Baptista*, Edward P. Myers, III[1]

OGI School of Science & Engineering, Oregon Health & Science University, 20000 NW Walker Road, Beaverton, OR 97006, USA

Abstract

Challenges posed by the Columbia River estuary–plume–shelf system have led to the development of ELCIRC, a model designed for the effective simulation of 3D baroclinic circulation across river-to-ocean scales. ELCIRC uses a finite-volume/finite-difference Eulerian–Lagrangian algorithm to solve the shallow water equations, written to realistically address a wide range of physical processes and of atmospheric, ocean and river forcings. The numerical algorithm is volume conservative, stable and computationally efficient, and it naturally incorporates wetting and drying of tidal flats. ELCIRC has been subject to systematic benchmarking, and applied to the description of the Columbia River circulation. This paper motivates and describes the formulation, presents and critically analyzes the results of selected benchmarks, and introduces ELCIRC as an open-source code available for community use and enhancement. A companion paper describes the application of ELCIRC to the Columbia River.

Keywords: Mathematical modeling; Ocean, coastal and estuarine circulation; Eulerian lagrangian methods; Finite volumes; Finite differences; Semi-implicit methods

1. Introduction

Tightly coupled estuary–plume–shelf systems pose cross-scale modeling challenges that are still insufficiently addressed by the communities developing open-source marine models such as POM (Blumberg and Mellor, 1987; Oey and Mellor, 1993), ROMS (Haidvogel et al., 2000), SEOM (Iskandarani et al., 2003) and QUODDY (Lynch et al., 1996). To illustrate these challenges, we consider briefly the Columbia River, a complex system that requires extensive, systematic modeling due to its central role in the economy and way of life of the Pacific Northwest of the United States.

*Corresponding author. Tel.: +1-503-748-1147; fax: +1-503-748-1273.

E-mail address: baptista@ccalmr.ogi.edu (A.M. Baptista).

[1]Now at National Ocean Service, NOAA, Office of Coastal Survey, Silver Spring, MD 20910-3282, USA.

0278-4343/$ - see front matter © 2004 Elsevier Ltd. All rights reserved.
doi:10.1016/j.csr.2004.07.021

With the second largest annual river discharge in the United States, the Columbia River is subject to highly variable forcings from river, ocean and atmosphere, and is characterized by a rich diversity of circulation regimes and by strong physical gradients. The freshwater plume is a major regional oceanographic feature, controlled at various scales by coastal winds, freshwater discharges, tides and bathymetry. The estuary is shallow, except for two deep channels—the longest of which acts as the major conduit for freshwater discharge. Extensive wetting and drying (e.g., Fig. 1a, b) occurs both in the estuary main stem and in ecologically important lateral bays. In the channels, velocities may reach 5 m/s in ebb, and tidal ellipses are topographically constrained. Hydraulic residence times are short, and residual velocities are strong and highly variable in space and time. Salinity intrusion is compressed, reaching at most about 48 km upstream of the mouth, while tidal influence is felt all the way to the first dam, 232 km upstream. Strong, largely salinity-driven stratification fosters complex and highly variable baroclinic circulation patterns, and creates the opportunity for estuarine turbidity maxima to develop in both channels of the main stem.

The dynamics of the plume and the estuary are inextricably linked, through active tidal exchange and strong frontal structures extending across the mouth (Fig. 1c, d). Shelf winds dramatically affect the low-frequency water levels in the estuary. Through both upwelling and control of plume orientation and attachment to the coast, shelf

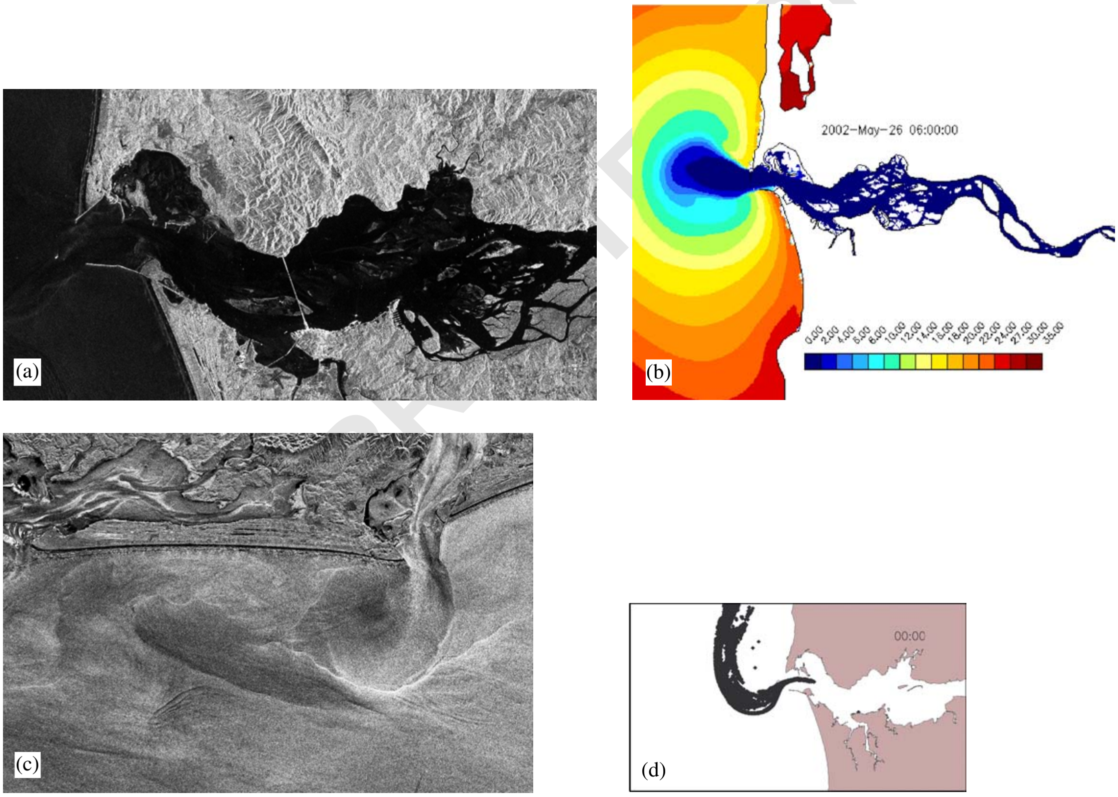

Fig. 1. Among the many modeling challenges posed by the Columbia River are the extensive wetting and drying of estuarine tidal flats (a. SAR image; b. ELCIRC salinity simulation, with white areas showing drying of tidal flats) and the tight interconnectivity of estuarine and plume processes and features, including fronts (c. SAR image; d. ELCIRC simulations showing fronts through loci of 10,000 particles after 48 h of dispersal). SAR images are © Canadian Space Agency 2002, and are shown courtesy of the NOAA Comprehensive Large Array-data Stewardship System (CLASS).

winds also impact estuarine budgets of heat and salt.

Systematic, detailed numerical modeling of the Columbia River is being conducted in the context of CORIE, a multi-purpose coastal margin observatory (Baptista et al., 1998; Baptista et al., 1999; Baptista, 2002) that produces both daily forecasts and multi-year hindcast simulations. We recognized early on that setting a boundary condition at or near the mouth of the Columbia River would be a daunting challenge (e.g., Fig. 1c, d), with unlikely odds of success—and thus we made the decision to model the estuary and plume (thus, the shelf) as a whole. This was also most consistent with the scientific and management issues that the CORIE modeling system is designed to address.

The broad context of the CORIE goals, the complexity of the Columbia River, and the decision to address the Columbia River dynamics across estuarine–plume–shelf scales, combine to create a set of challenging modeling requirements, including:

- Covering geographically extensive domains (river-to-ocean scales), while retaining high spatial resolutions in multiple localized regions.
- Covering multiple decades, at sub-hour resolution.
- Enabling state-of-the-art 3D representations of riverine, estuarine and ocean circulation processes, including advection-dominated flows, sharp density gradients, and wetting and drying.
- Achieving sufficient computational efficiency to enable both operational forecasting and creation of long-term (multi-year) simulation databases, without sacrificing process representation or space–time resolution.

Early attempts by our group to use established models such as ADCIRC (Luettich et al., 1991), POM and QUODDY did not meet the above requirements (unpublished work); reasons varied, but commonly included cost inefficiencies due to time step constraints associated with the treatment of advection. Circa (1999), an extensive review of the existing literature, revealed the existence of an unstructured-grid code (UnTrim, Casulli and Zanolli, 1998) the numerical strategy of which—and, in particular, the treatment of advection—appeared ideally suited for the task. However, neither UnTRIM nor its earlier, structured-grid version (TRIM, Casulli and Cheng, 1992) were available as free, open source software. UnTRIM also did not include a baroclinic component[2] and both UnTRIM and TRIM were overly simplistic relative to physical processes such as turbulence (e.g., direct specification of vertical mixing[2]) and air–water exchanges (e.g., no heat balance terms), which are essential in the Columbia River and in many other marine modeling applications.

We have since undertaken the development of ELCIRC, inspired by the UnTRIM formulation, but independently coded and with expanded process representation. Like UnTRIM, ELCIRC solves the shallow water equations using a semi-implicit Eulerian–Lagrangian finite volume/finite difference method reliant on horizontally unstructured grids and unstretched z-coordinates. However, ELCIRC differs algorithmically from UnTRIM in the treatment of tangential velocities and of transport quantities (salinity and temperature). In addition, ELCIRC allows for the use of state-of-the-art turbulence closure schemes (Umlauf and Burchard, 2003), includes terms for the tidal potential and atmospheric pressure gradients, and provides a detailed description of air–water exchanges (see Appendix A).

ELCIRC has been subject to extensive benchmarking and has been applied to the description of important Columbia River features and processes. A limited number of researchers have used ELCIRC in other applications (Robinson et al., 2004; Myers and Aikman, 2003; and Pinto et al., 2003). Based on the benchmarks and pilot applications, our current assessment is that ELCIRC is a functional code, generally well adjusted to the modeling requirements that we set forth, and with contrasting characteristics relative to existing coastal circulation community models, especially in the treatment of advection and wetting-and-drying, and in the order of conver-

[2]Baroclinic terms and Mellor and Yamada (1982) turbulence closure equations have recently been included in UnTRIM (V. Casulli, private communication).

gence of the numerical solution. As a natural next step, ELCIRC is being released as an open-source code (CCALMR, 2003), with the expectation that it will anchor a modeling framework that will evolve in robustness and disciplinary scope.

The present paper constitutes a comprehensive reference for version 5.01 of ELCIRC (henceforth, ELCIRC_v5.01), describing its formulation and critically presenting the solution of several synthetic but demanding benchmarks. A companion paper (Baptista et al., 2004) will describe in detail aspects of the simulation of the 3D baroclinic circulation in the Columbia River estuary and plume—by far the most extensive application of ELCIRC to date.

After this Introduction, Section 2 presents the physical and mathematical formulation of the model, with the air–water exchange formulation summarized in Appendix A. The numerical strategy is detailed in Section 3, and Section 4 describes the performance of ELCIRC against a range of synthetic benchmark tests. Finally, Section 5 presents a road map for future developments.

2. Physical formulation

2.1. Governing equations

We solve for the free surface elevation, 3D water velocity, salinity and temperature, using a set of six hydrostatic equations based on the Boussinesq approximation, which represent mass conservation (in both 3D and depth-integrated forms), momentum conservation, and conservation of salt and heat:

$$\frac{\partial u}{\partial x}+\frac{\partial v}{\partial y}+\frac{\partial w}{\partial z}=0, \tag{1}$$

$$\frac{\partial \eta}{\partial t}+\frac{\partial}{\partial x}\int_{H_R-h}^{H_R+\eta} u\,\mathrm{d}z+\frac{\partial}{\partial y}\int_{H_R-h}^{H_R+\eta} v\,\mathrm{d}z=0, \tag{2}$$

$$\frac{\mathrm{D}u}{\mathrm{D}t}=fv-\frac{\partial}{\partial x}\left\{g(\eta-\alpha\hat{\psi})+\frac{P_a}{\rho_0}\right\}-\frac{g}{\rho_0}\int_z^{H_R+\eta}\frac{\partial\rho}{\partial x}\mathrm{d}z +\frac{\partial}{\partial z}\left(K_{mv}\frac{\partial u}{\partial z}\right)+F_{mx}, \tag{3}$$

$$\frac{\mathrm{D}v}{\mathrm{D}t}=-fu-\frac{\partial}{\partial y}\left\{g(\eta-\alpha\hat{\psi})+\frac{P_a}{\rho_0}\right\}-\frac{g}{\rho_0}\int_z^{H_R+\eta}\frac{\partial\rho}{\partial y}\mathrm{d}z +\frac{\partial}{\partial z}\left(K_{mv}\frac{\partial v}{\partial z}\right)+F_{my}, \tag{4}$$

$$\frac{\mathrm{D}S}{\mathrm{D}t}=\frac{\partial}{\partial z}\left(K_{sv}\frac{\partial S}{\partial z}\right)+F_s, \tag{5}$$

$$\frac{\mathrm{D}T}{\mathrm{D}t}=\frac{\partial}{\partial z}\left(K_{hv}\frac{\partial T}{\partial z}\right)+\frac{\dot{Q}}{\rho_0 C_p}+F_h, \tag{6}$$

where

(x, y)	horizontal Cartesian coordinates, (m)
(ϕ, λ)	latitude and longitude
z	vertical coordinate, positive upward, (m)
t	time, (s)
H_R	z-coordinate at reference level (geoid or mean sea level (MSL))
$\eta(x,y,t)$	free-surface elevation, (m)
$h(x,y)$	bathymetric depth, (m)
$\vec{u}(\vec{x},t)$	water velocity at $\vec{x}=(x,y,z)$, with Cartesian components (u,v,w), $(\mathrm{m\,s^{-1}})$
f	Coriolis factor, $(\mathrm{s^{-1}})$ (Section 2.5)
g	acceleration of gravity, in $(\mathrm{m\,s^{-2}})$
$\hat{\psi}(\phi,\lambda)$	tidal potential, (m) (Section 2.5)
α	effective Earth elasticity factor ($\approx$0.69; Foreman et al., 1993)
$\rho(\vec{x},t)$	water density; by default, reference value ρ_0 is set as $1025\,\mathrm{kg\,m^{-3}}$
$P_a(x,y,t)$	atmospheric pressure at the free surface, $(\mathrm{N\,m^{-2}})$
S, T	salinity and temperature of the water (practical salinity units (psu), °C)
K_{mv}	vertical eddy viscosity, $(\mathrm{m^2\,s^{-1}})$
K_{sv}, K_{hv}	vertical eddy diffusivity, for salt and heat, $(\mathrm{m^2\,s^{-1}})$
F_{mx}, F_{my}, F_s, F_h	horizontal diffusion for momentum and transport equations
$\dot{Q}(\phi,\lambda,z,t)$	rate of absorption of solar radiation $(\mathrm{W\,m^{-2}})$
C_p	specific heat of water $(\mathrm{J\,kg^{-1}\,K^{-1}})$

In the remainder of this text and in most ELCIRC simulations, we neglect horizontal diffusion in the momentum and transport equations. Horizontal diffusion tends to be a secondary process, and the solution method introduces numerical horizontal diffusion that may exceed its physical counterpart (see further discussion in Sections 3.4 and 4.1.3). The reader is referred to Casulli and Zanolli (1998) and Casulli and Cheng (1992) for a treatment of horizontal diffusion terms in the framework of Eulerian–Lagrangian finite volume models.

The differential system for the six primary variables (η, u, v, w, T, S), Eqs. (1)–(6), is closed with the equation of state (density as a function of salinity and temperature; Section 2.2), the definition of the tidal potential and Coriolis factor (Section 2.5), parameterizations for vertical mixing (Section 2.4), and appropriate initial and boundary conditions. Initial conditions require problem-dependent specification of pre-simulation fields of all primary variables and of any turbulence parameters required by the vertical mixing parameterization. We will discuss the vertical boundary conditions in Section 2.3. Lateral boundary conditions may be chosen from a range of Dirichlet, Neumann and open boundary conditions.

2.2. Equation of state

The density of sea water is defined as a function of salinity, temperature and hydrostatic pressure, using the International Equation of State of Sea Water (ISE80) standard described in Millero and Poisson (1981):

$$\rho(S,T,p) = \frac{\rho(S,T,0)}{\left[1 - 10^5 p/K(S,T,p)\right]}, \tag{7}$$

where $\rho(S,T,0)$ (kg/m$^{-3)}$ is the density at one standard atmosphere, and $K(S,T,p)$ is the secant bulk modulus. Polynomial expressions for both $\rho(S,T,0)$ and $K(S,T,p)$ are integral to the ISE80 standard, and will not be repeated here. We compute the water pressure in *bars*, consistent with the hydrostatic approximation:

$$p = 10^{-5} g \int_z^{H_R+\eta} \rho(S,T,p)\,\mathrm{d}z. \tag{8}$$

2.3. Vertical boundary conditions for primary equations

2.3.1. Horizontal momentum: surface boundary

At the sea surface, we enforce the balance between the internal Reynolds stress and the applied shear stress, i.e.

$$\rho_0 K_{mv} \left(\frac{\partial u}{\partial z}, \frac{\partial v}{\partial z}\right) = (\tau_{Wx}, \tau_{Wy}) \quad \text{at} \quad z = H_R + \eta. \tag{9}$$

ELCIRC allows for two different approaches to the parameterization of spatially and temporally variable surface shear stresses. One approach consists of the use of a bulk aerodynamic algorithm developed by Zeng et al. (1998) to account for ocean surface fluxes (momentum, heat and salt) under various conditions of stability of the atmosphere. This approach is summarized in Appendix A, and is recommended when ELCIRC is used in conjunction with (or, more commonly, forced by outputs from) an atmospheric model.

Short of detailed information on atmospheric stability, surface stresses can alternatively be evaluated as

$$(\tau_{Wx}, \tau_{Wy}) = \rho_a C_{Ds} |\vec{W}| (W_x, W_y) \tag{10}$$

where, ρ_a is the air density (kgm^{-3}), C_{Ds} the wind drag coefficient (–), $\vec{W}(x,y,t)$ the wind velocity at 10 m above the sea surface, with magnitude $|W|$ and components W_x and W_y (ms^{-1})

and where:

$$C_{Ds} = 10^{-3}(A_{W1} + A_{W2}|\vec{W}|) \quad \text{if} \quad W_{low} \leqslant |\vec{W}| \leqslant W_{high} \tag{11}$$

with C_{Ds} held constant (at either W_{low} or W_{high} values) outside the range, as appropriate. For moderately strong winds, this formula allows the efficiency of the air–ocean transfer of momentum to increase with increasing wind speed. Many alternative literature values have been proposed for A_{W1}, A_{W2} and associated ranges of validity (e.g., see review in Pond and Pickard (1998), pp. 135–137). In the absence of data to the contrary, ELCIRC assumes, as the starting point for site-specific calibration, that

$$A_{W1} = 0.61,$$
$$A_{W2} = 0.063,$$
$$W_{low} = 6,$$
$$W_{high} = 50. \quad (12)$$

2.3.2. Horizontal momentum: bottom boundary

As customary, we enforce at the sea bottom the balance between the internal Reynolds stress and the bottom frictional stress, i.e.

$$\rho_0 K_{mv}\left(\frac{\partial u}{\partial z}, \frac{\partial v}{\partial z}\right)_b = (\tau_{bx}, \tau_{by}), \quad \text{at} \quad z = H_R - h, \quad (13)$$

where the bottom stress is defined as

$$(\tau_{bx}, \tau_{by}) = \rho_0 C_{Db}\sqrt{u_b^2 + v_b^2}(u_b, v_b). \quad (14)$$

The bottom drag coefficient C_{Db} is typically variable in space, and might also vary at various temporal scales (e.g., through current–wave interactions or long-term changes in bottom texture). Site-specific calibration is often required. In ELCIRC, the bottom drag coefficient can be externally specified, or can be evaluated internally by matching velocities (u_b,v_b) at or near the edge of the bottom boundary layer:

$$C_{Db} = \max\left\{\left(\frac{1}{\kappa}\ln\frac{\delta_b}{z_0}\right)^{-2}, C_{Dbmin}\right\}, \quad (15)$$

where $\kappa = 0.4$ is the von Karman's constant, z_0 the local bottom roughness, and δ_b half the thickness of the bottom computational cell. The parameter z_0 depends on the local bottom roughness, and is typically of the order of 1 cm (Blumberg and Mellor, 1987). A coarse bottom discretization may greatly overestimate δ_b relative to the true boundary layer thickness and, without the moderating effect of C_{Dbmin}, could grossly underestimate C_{Db}. Values of C_{Dbmin} of 0.0075 and 0.0025 have been recommended for continental shelves (Lynch et al., 1996) and deep ocean (Blumberg and Mellor, 1987), respectively, corresponding to an "effective δ_b" of approximately 1 and 30 m. Ultimately, the choice is site-specific and spatially variable.

2.3.3. Heat and salt conservation

In most cases, there are no salt fluxes across the sea surface and bottom, neither is there any heat flux at the bottom. However, heat exchanges through the air–sea interface are important in most coastal and ocean systems. While solar radiation is treated directly in Eq. (6), all other heat exchanges must be accounted through the surface boundary condition. Specifically:

$$K_{hv}\frac{\partial T}{\partial z} = \frac{H_{tot}^* \downarrow}{\rho_0 C_p}, \quad \text{at } z = H_R + \eta, \quad (16)$$

where $H_{tot}^* \downarrow$ is the net downwards heat flux at the air–water interface, exclusive of solar radiation (see Appendix A).

2.4. Parameterization of turbulent vertical mixing

Recognizing that the parameterization of turbulent vertical mixing remains an open question in coastal modeling, we allow for multiple choices among many approaches of widely varying complexity that have been proposed in the literature. Currently coded are a zero-equation model (based on Pacanowski and Philander, 1981) and multiple two-and-a-half equation models (Umlauf and Burchard (2003) and Mellor and Yamada (1982), as modified by Galperin et al. (1988)). In all approaches, we assume similarity of the vertical mixing for heat and salt, i.e.$K_{sv} \cong K_{hv}$.

2.4.1. Zero-equation models

Several zero-equation parameterizations attempt to account for the effect of varying stratification on the vertical mixing. Vaz and Simpson (1994) compared three such schemes (Munk and Anderson, 1948; Pacanowski and Philander, 1981; Lehfeldt and Bloss, 1988) among each other and against simpler (constant and step-function viscosities) and more complex approaches (one- and two-equation schemes, from Mellor and Yamada, 1982). The comparison, set up in a context of transient estuarine stratification problems and based on qualitative and quantitative tests, found the scheme of Pacanowski and Philander (1981) to perform the best among zero-equation closures.

The scheme assumes that the local eddy viscosity and diffusivity, K_{mv} and K_{hv}, only depend on the gradient Richardson number, Ri. Specifically,

$$K_{mv} = \frac{v_0}{(1+5Ri)^2} + v_b, \tag{17}$$

$$K_{hv} = \frac{K_{mv}}{1+5Ri} + K_b, \tag{18}$$

where K_{mv} and K_{hv} approach a turbulent upper value,v_0, in the limit of no density stratification and finite vertical shear (i.e., $Ri \to 0$), and approach molecular background values,$v_b$and K_b, in the limit of large density stratification (i.e., $Ri \to \infty$). While Pacanowski and Philander (1981) recommended $v_0 = 5\times10^{-3}$, $v_b = 10^{-4}$ and $K_b = 10^{-5}\,\mathrm{m^2\,s^{-1}}$, ELCIRC gives the user the choice on these values. In the above equations, the Richardson number is defined as

$$Ri = \frac{N^2}{(\partial u/\partial z)^2 + (\partial v/\partial z)^2}, \tag{19}$$

where the Brunt–Vassala frequency, N^2, can be negative:

$$N^2 = \frac{g}{\rho_0}\frac{\partial \rho}{\partial z}. \tag{20}$$

2.4.2. Two-and-a-half equation models

We have implemented in ELCIRC both the traditional 2.5 closure model of Mellor and Yamada (1982) as modified by Galperin et al. (1988) (hereafter, MY25), and the generic length scale (GLS) closure model proposed by Umlauf and Burchard (2003). GLS includes, as particular realizations, a variety of two-and-a-half equation models, both new (e.g., GLS as optimized by Umlauf and Burchard (2003), henceforth UB) and traditional—such as $k-\varepsilon$ (kinetic energy and energy dissipation, Rodi (1984)) and $k-\omega$ (kinetic energy and frequency of dissipation, Wilcox, 1998). Although the GLS framework does not strictly include MY25, it allows for an analog ($k-k\ell$; kinetic energy and kinetic energy times length scale).

Central to the GLS framework are two equations that govern the transport, production and dissipation of the turbulent kinetic energy (k) and of a generic length-scale variable (ψ):

$$\frac{\mathrm{D}k}{\mathrm{D}t} = \frac{\partial}{\partial z}\left(v_k^{\psi}\frac{\partial k}{\partial z}\right) + K_{mv}M^2 + K_{hv}N^2 - \varepsilon, \tag{21}$$

$$\frac{\mathrm{D}\psi}{\mathrm{D}t} = \frac{\partial}{\partial z}\left(v_{\psi}\frac{\partial \psi}{\partial z}\right) + \frac{\psi}{k}(c_{\psi1}K_{mv}M^2 + c_{\psi3}K_{hv}N^2 - c_{\psi2}F_w\varepsilon), \tag{22}$$

where $c_{\psi1}$, $c_{\psi2}$ and $c_{\psi3}$are model-specific constants (Table 1), F_w is a wall proximity function, M and N are shear and buoyancy frequencies, and ε is the dissipation rate. The following definitions apply

$$M^2 = \left(\frac{\partial u}{\partial z}\right)^2 + \left(\frac{\partial v}{\partial z}\right)^2, \quad \varepsilon = (c_{\mu}^0)^3 k^{1.5+m/n}\psi^{-1/n} \tag{23}$$

with the constant c_{μ}^0 set at $\sqrt{0.3}$.

The generic length scale is defined as

$$\psi = (c_{\mu}^0)^p k^m \ell^n, \tag{24}$$

where the choice of the constants p, m and n determines the specific closure model (Table 1). The desired vertical viscosities and diffusivities are related to k, ψ, and stability functions, in the form:

Table 1
Constants for various GLS closure models

	ψ	p	m	n	σ_k^{ψ}	σ_{ψ}	$c_{\psi1}$	$c_{\psi2}$	$c_{\psi3}^{+}$	$c_{\psi3}^{-}$ [a]	F_w
$k-\varepsilon$	$\sim\varepsilon$	3	1.5	−1	1.0	1.3	1.44	1.92	1·0	−0·629	1
$k-k\ell$	$k\ell$	0	1	1	1.96	1.96	0.9	0.5	1·0	0.9	Eq. (29)
$k-\omega$	$\sim\sqrt{k}/\ell$	−1	0.5	−1	2.0	2.0	0.555	0.833	1·0	−0·642	1
UB	$\sim k/\ell^{2/3}$	2	1	−0.67	0.8	1.07	1	1.22	1·0	0.05	1

[a]Values reflect the choice of stability functions from Kantha and Clayson (1994).

$$K_{mv} =; c_\mu k^{1/2}\ell,\ K_{hv} = c'_\mu k^{1/2}\ell,$$

$$\nu_k^\psi = \frac{K_{mv}}{\sigma_k^\psi},\ \nu_\psi = \frac{K_{mv}}{\sigma_\psi}, \tag{25}$$

where ν_k^ψ and ν_ψ. are vertical turbulent diffusivities for k and ψ, and the Schmidt numbers σ_k^ψ and σ_ψ are model-specific constants (Table 1). An algebraic stress model (e.g. Kantha and Clayson, 1994; Canuto et al., 2001; or Galperin et al., 1988) is required to define the stability functions. Using Kantha and Clayson (1994), the stability functions assume the form

$$c_\mu = \sqrt{2}s_m \quad c'_\mu = \sqrt{2}s_h, \tag{26}$$

with

$$s_h = \frac{0.4939}{1-30.19G_h}, \quad s_m = \frac{0.392+17.07s_hG_h}{1-6.127G_h},$$

$$G_h = \frac{G_{h\_u}-(G_{h\_u}-G_{h\_c})^2}{G_{h\_u}+G_{h0}-2G_{h\_c}} \tag{27}$$

and

$$G_{h\_u} = \min\left(G_{h0}, \max\left(-0.28, \frac{N^2\ell^2}{2k}\right)\right),$$

$$G_{h0} = 0.0233,\ G_{h\_c} = 0.02. \tag{28}$$

The wall proximity function, F_w, allows models with a positive n (such as the MY25 analog, $k-k\ell$) to satisfy boundary conditions. F_w is trivially unity for models with a negative n. For $k-k\ell$,

$$F_w = 1 + 1.33\left[\frac{\ell}{\kappa d_b}\right]^2 + 0.25\left[\frac{\ell}{\kappa d_s}\right]^2, \tag{29}$$

where d_b and d_s are, respectively, the distance to the computational bottom and to the sea surface:

$$d_b(x,y) = z - [H_R - h(x,y)], \tag{30}$$

$$d_s(x,y) = H_R + \eta(x,y) - z. \tag{31}$$

Table 1 shows the choices of constants p, m and n associated with four common GLS options, the resulting form of ψ, and the values of the constants $c_{\psi1}$, $c_{\psi2}$, $c_{\psi3}$, σ_k^ψ and σ_ψ. Note that different values of the buoyancy parameter $c_{\psi3}$ are used for stable ($c_{\psi3}^-$) and unstable ($c_{\psi3}^+$) stratification. It is important to recognize that, for all models, limits on length scales are applied at several stages of the calculations, to ensure that mixing remains positive. The choice of these limits is practically important, yet theoretically ambiguous. While we in general follow the recommendations of Warner et al. (2004), we deviate from them in adopting the same lower bound for ψ across all models, rather than model-specific bounds. Specifically, we use $\psi_{min} = 10^{-8}$ (the value recommended by Warner et al. (2004) for $k-k\ell$). We found this common lower bound for ψ important to ensure consistency across closure models, in the context of the solution of selected benchmarks (e.g., Section 4.3).

Regardless of the specific closure model, the solution of Eqs. (21) and (22) requires boundary conditions at the free surface and the computational bottom. Rather conventionally, these boundary conditions specify turbulent kinetic energy as a function of the frictional velocities at the appropriate surface, in the form:

$$k = \frac{16.6^{2/3}}{2}u_*^2 = \frac{16.6^{2/3}}{2}K_{mv}\sqrt{\left(\frac{\partial u}{\partial x}\right)^2 + \left(\frac{\partial v}{\partial y}\right)^2}, \tag{32}$$

and specify ψ (note Eq. (24)) by additionally setting the mixing length to the distances to the free surface

$$\ell = \kappa d_b \text{ or } \kappa d_s. \tag{33}$$

We stated earlier that MY25 is not considered a special case of GLS. Consistent with this view, the ELCIRC implementation of MY25 is rather conventional (Mellor and Yamada (1982), as modified by Galperin et al. (1988)), and is coded independently of GLS. Yet, it is important to recognize that the main difference between MY25 and GLS is arguably in details of the internally imposed length-scale limits: in MY25 the length scale is only limited in the calculation of stability functions, while in GLS the length scale is limited in the calculation of production, wall proximity function, and stability functions (Warner et al., 2004). Other significant differences between MY25 and GLS include the stability functions (Galperin et al. (1988) versus multiple options, such as our choice of Kantha and Clayson (1994)) and the buoyancy parameter $c_{\psi3}$ (constant at 0.9 versus dependent on stratification stability, Table 1).

2.5. Definition of Coriolis factor and tidal potential

Rather conventionally, the earth rotation is represented through the Coriolis acceleration in the momentum equations. The Coriolis factor, f, is a well known function of latitude,ϕ:

$$f(\phi) = 2\Omega \sin \phi, \tag{34}$$

where $\Omega = 7.29 \times 10^{-5}\,\mathrm{rad\,s^{-1}}$ is the angular velocity of rotation of the earth. To minimize coordinate inconsistencies (Cartesian in ELCIRC, spherical in Eq. (34)), we use a *β-plane approximation* for f:

$$f = f_C + \beta_C(y - y_C), \tag{35}$$

where subscript C denotes the mid-latitude of the domain and β is the local derivative of the Coriolis factor.

The tidal potential is defined following Reid (1990):

$$\hat{\psi}(\phi, \lambda, t) = \sum_{n,j} C_{jn} f_{jn}(t_0) L_j(\phi) \cos\left[\frac{2\pi(t - t_0)}{T_{jn}} + j\lambda + v_{jn}(t_0)\right], \tag{36}$$

where

C_{jn} constants (e.g., Reid (1990)) characterizing the amplitude of tidal constituent n of species j ($j=0$, declinational; $j=1$, diurnal; $j=2$, semi-diurnal), (m)
t_0 reference time
$f_{jn}(t_0)$ nodal factors
$v_{\mathrm{jn}}(t_0)$ astronomical arguments, (r)
$L_j(\phi)$ species-specific coefficients ($L_0 = \sin^2\phi$; $L_1 = \sin(2\phi)$; $L_2 = \cos^2\phi$)
T_{jn} period of constituent n of species j

3. Numerical algorithm

3.1. Overview

The numerical algorithm of ELCIRC follows the functional sequence illustrated in Fig. 2, and has the following important features:

1. A semi-implicit scheme is used: (a) the barotropic pressure gradient in the momentum equation and the flux term in the continuity equation are treated semi-implicitly, with implicitness factor $0.5 \leqslant \theta \leqslant 1$; (b) the vertical viscosity term and the bottom boundary condition for the momentum equations are treated fully implicitly; and (c) all other terms are treated explicitly. This ensures both stability (Casulli and Cattani, 1994) and computational efficiency.
2. The normal component of the horizontal momentum equations is solved simultaneously with the depth-integrated continuity equation, i.e., there is no mode splitting between these equations. The total derivatives of the normal velocity are discretized using Lagrangian backtracking, thus preventing advection from imposing stability constraints on the time step.
3. The vertical velocity is solved from the 3D continuity equation using a finite volume approach.
4. The tangential component of the horizontal momentum equations is formally solved with finite differences. The solution is computationally efficient, because we re-use matrices formed and inverted in the process of computing normal velocities.
5. Once the full 3D velocity is recovered, the transport equations for salinity and temperature are solved at *both* the polygonal vertices (nodes) and centers of element sides, using finite differences. This amounts to splitting each element in the flow grid into four transport sub-elements, and reduces numerical diffusion. The solution requires backtracking along characteristic lines, which is done anew (i.e., without re-using the backtracking for normal velocities) to account for the most recent flow field. After the salinity and temperature are found, the density is calculated from the equation of state, and is fed back to the momentum equations at the next time step (i.e., the baroclinic term is treated fully explicitly).
6. If a two-and-a-half equation turbulence closure is invoked, the eddy viscosity and diffusivity are computed at each time step prior to the solution

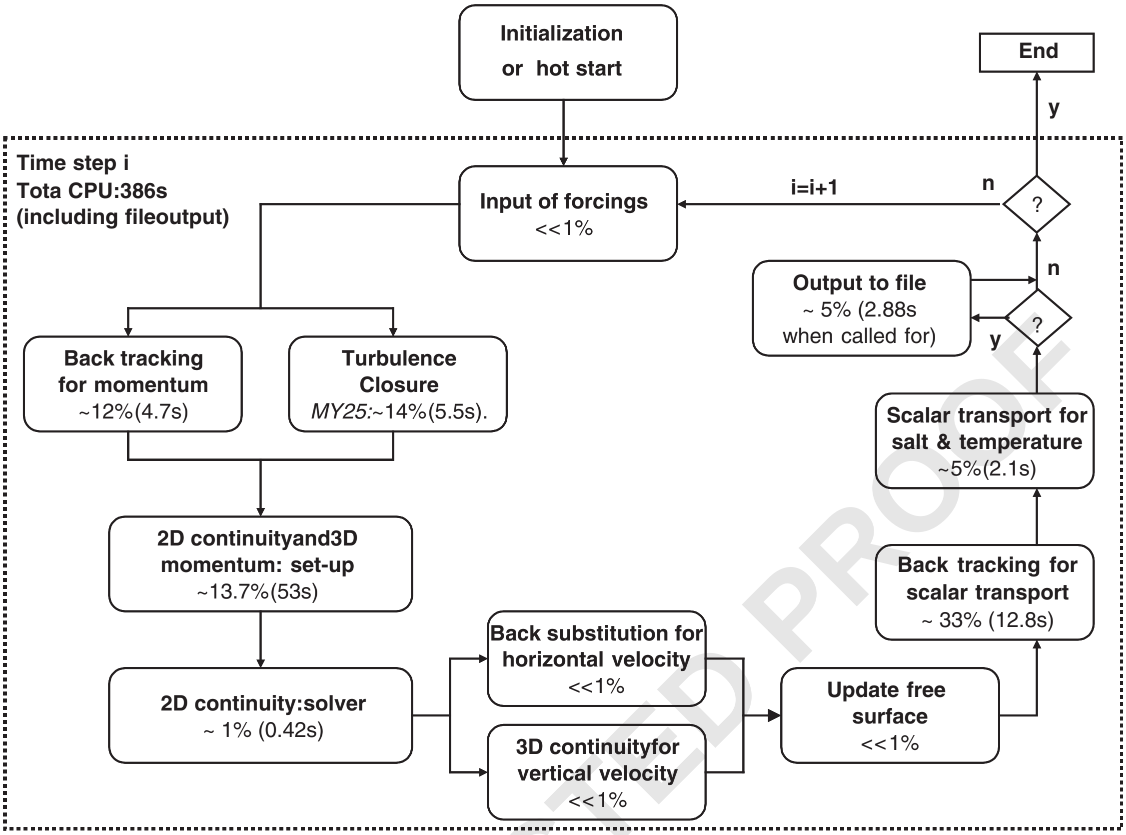

Fig. 2. Functional sequence of the ELCIRC solution, and percentages of CPU used by major tasks. Note: Relative CPU varies with the specific application. Numbers shown are for a time step with file output, within a recent river-to-ocean simulation of 3D baroclinic Columbia River circulation (Baptista et al.)), in a single processor of a dual-processor 2.4 GHz, 4 Gb, Intel Xeon. The grid has 33,634 horizontal nodes, 50,389 horizontal elements and 62 vertical layers, for a total of ≈2.2 M active prism faces.

of the momentum equation, using information from the previous time step.

Features 1–3 follow Casulli and Zanolli (1998) closely, while features 4–6 are deviations from TRIM/UnTRIM strategies that we found useful in controlling numerical diffusion (feature 5, cf. Section 4.1.3), improving the representation of Coriolis (feature 4, cf. Sections 4.2.1 and 4.2.2) and providing qualitatively realistic representations of plume dynamics (features 4–6, cf. Section 4.4).

3.2. Domain discretization

The 3D domain is discretized into a series of layers in the vertical and into a combination of triangular and/or quadrangular elements in the horizontal (Fig. 3a). Unstretched z-coordinates are used,[3] with each layer extending throughout the entire horizontal domain and being numbered sequentially upwards. The thickness of the kth layer (i.e., the distance between levels $k-1$ and k) is Δz_k, and the distance between half-levels is $\Delta z_{k+1/2} = (\Delta z_k + \Delta z_{k+1})/2$. Note that the thicknesses of the bottom and top layers include only the portions occupied by water.

[3] The choice of z-coordinates enables a natural treatment of wetting and drying, but creates a stair-case representation of the bottom that limits the representation of the bottom boundary layer. A generalized sigma coordinate (cf. Song and Haidvogel, 1994) is being considered as an option for ELCIRC, but has not yet been implemented.

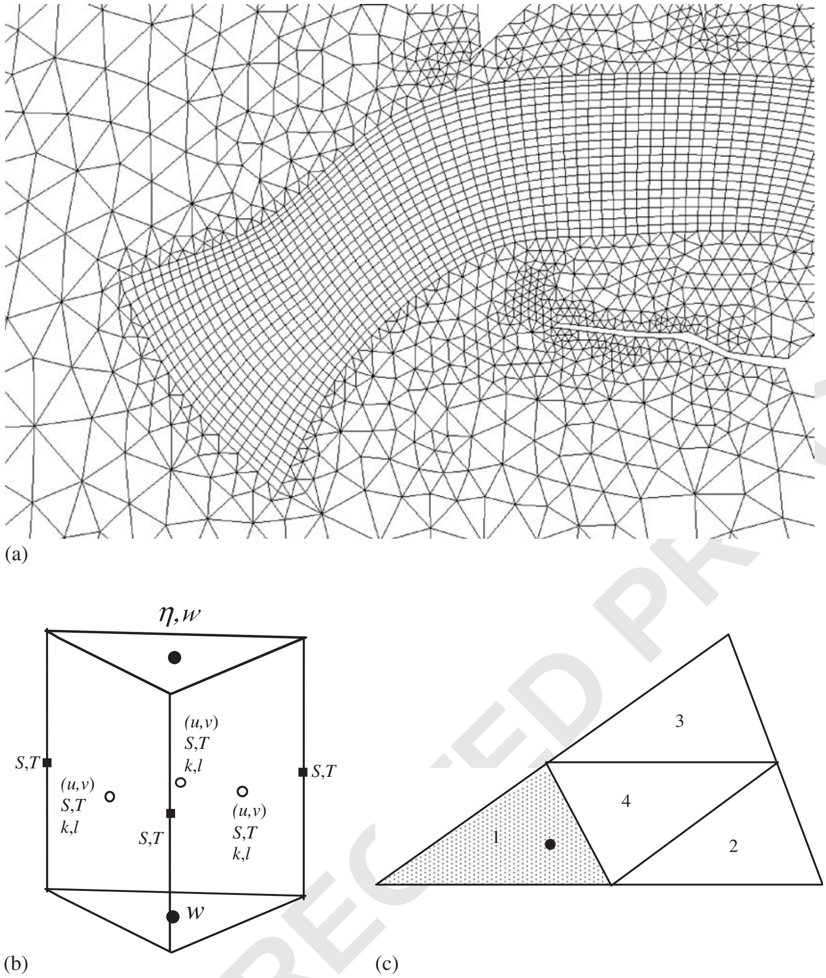

Fig. 3. ELCIRC grids are unstructured in the horizontal, with combinations of triangles and quadrangles (a), and use unstretched z-coordinates in the vertical. As shown in (b), most variables (horizontal velocities, salinity, temperature and turbulent quantities) are defined at half levels, either (or both) at nodes or side centers; water levels and vertical velocities are however defined at full levels, and element centers. The definition of salinity and temperature at both nodes and side centers effectively means that horizontal elements are split into four sub-elements for the purpose of solving the scalar-transport equations; for instance, interpolation at the foot of the characteristic line shown in (c) is based only on sub-element 1.

The combined horizontal and vertical discretizations result in the whole 3D domain being divided into a series of prisms. The depths at each side, calculated from depths at nodes, are assumed to be constant, and the depths in each element are taken to be the maximum of depths at its sides. This results in a staircase representation of the bottom. Since the layer thicknesses at sides, elements, and nodes are in general different from each other, superscripts "e" and "p" are added to Δz to denote the elements and nodes, while Δz is reserved for sides. Some of the other notations to be used are:

N_p	number of nodes (vertices) in the horizontal grid
N_v	number of levels in the vertical grid
N_e	number of elements in the horizontal grid

N_s number of sides in the horizontal grid
$js(i,j)$ $(j=1, \ldots, i34(i))$ sides of element
$i34(i)$ number of sides in element i
$is(j,i)$ $(i=1,2)$ two elements that share side j
$ip(j,i)$ $(i=1,2)$ two end nodes of side j
l_j length of side j
P_i area of element i
δ_j distance between the two element centers sharing side j
m_j $(m_j^e;\ m_j^p)$ bottom level index for side (element/node) j
M_j $(M_j^e;\ M_j^p)$ free-surface level index for side (element/node) j.

We generally use subscripts for spatial location, and double subscripts for horizontal and vertical level indices.

A staggering scheme is used for the definition of variables (Fig. 3b). The elevation, defined at elemental centers, is assumed to be constant within each element. The normal and tangential components of the horizontal velocity, which are the actual unknowns to be solved from the momentum equations, are defined at the center of each vertical face of prism (i.e., at element side centers on half levels). The vertical velocity w is located at element centers on whole levels. The salinity, temperature and density are defined at vertices and side centers, for the reason outlined below.

As discussed by Casulli and Zanolli (1998), orthogonality[4] is, in a strict sense, a requirement for calculation of finite difference approximations of spatial gradients in unstructured grids. This requirement might in practice be relaxed, but the accuracy of solutions suffers from deviations from orthogonality. While a second-order accuracy can be achieved with uniform structured or unstructured orthogonal grids, only first-order accuracy is attainable with non-uniform orthogonal grids. For general non-orthogonal grids, the line connecting the two element centroids is not perpendicular to the common side, which is an additional source of errors.

Grid generation packages, including those typically used by the authors (Turner and Baptista (1991) and Zhang and Baptista (2000)), do not specifically ensure grid orthogonality. The burden of creating orthogonal or near-orthogonal grids is thus on the user, and is non- trivial for complex domains. In unconstrained parts of a computational domain, it is typically easy to generate orthogonal grids based on quadrangles. In more constrained regions, hybrid-element grids may be used to avoid major deviations from orthogonality (e.g., by selectively merging two non-orthogonal triangles into a quadrangle, within a region where the grid is predominantly formed by triangles).

3.3. Solving the depth-integrated continuity and horizontal momentum equations

A key to UnTRIM is that the solution of the depth-integrated continuity equation and horizontal momentum equations is conducted using local (element-side based) coordinate systems. Following Casulli and Zanolli (1998), we locally re-orient (x,y) such that the x-axis points outside of element $is\,(j,\,1)$, from the center of side j. Eqs. (3) and (4) are invariant under a rotation in the $(x,\,y)$ plane, and thus they retain their form under these local rotations. However, these equations now represent local conservation of normal and tangential momentum, respectively. For consistency, u and v refer from here onward to normal and tangential velocities.

Also, following Casulli and Zanolli (1998), we impose local (and thus global) volume conservation by using a semi-implicit finite-volume approach to integrate the continuity equation, Eq. (2), for element i:

$$P_i(\eta_i^{n+1}-\eta_i^n)+\theta\Delta t\sum_{l=1}^{i34(i)} s_{i,l}\ell_{jsj}\sum_{k=m_{jsj}}^{M_{jsj}}\Delta z_{jsj,k}^n u_{jsj,k}^{n+1}$$
$$+(1-\theta)\Delta t\sum_{l=1}^{i34(i)} s_{i,l}l_{jsj}\sum_{k=m_{jsj}}^{M_{jsj}}\Delta z_{jsj,k}^n u_{jsj,k}^n=0,$$
$$i=1,\ldots,N_e, \tag{37}$$

[4] Following Casulli and Zanolli (1998), a grid is defined as orthogonal if within each element a point ("center", although not necessarily the geometric center) can be identified such that the segment joining the centers of two adjacent elements, and the side shared by the two elements, have a non-empty intersection and are perpendicular to each other.

where θ is the implicitness factor for temporal discretization, $jsj = js(i,l)$ and $s_{i,l}$ is a sign:

$$s_{i,l} = \frac{is(jsj,1) + is(jsj,2) - 2i}{is(jsj,2) - is(jsj,1)}. \quad (38)$$

For stability reasons, a semi-implicit finite-difference scheme is used to solve the normal momentum equation for a side j:

$$\begin{aligned}
\Delta z_{j,k}^n (u_{j,k}^{n+1} - u_{j,k}^*) &= \Delta z_{j,k}^n f_j v_{j,k}^n \Delta t - \Delta z_{j,k}^n \frac{g\,\Delta t}{\delta_j}\Big[\theta\Big(\eta_{is(j,2)}^{n+1} - \eta_{is(j,1)}^{n+1}\Big) \\
&\quad +(1-\theta)\Big(\eta_{is(j,2)}^{n} - \eta_{is(j,1)}^{n}\Big)\Big] \\
&\quad - \Delta z_{j,k}^n \frac{g\Delta t}{\rho_0 \delta_j}\left[\sum_{l=k}^{M_j} \Delta z_l^n \Big(\rho_{is(j,2),l}^n - \rho_{is(j,1),l}^n\Big)\right. \\
&\quad \left. - \frac{\Delta z_{j,k}^n}{2}\Big(\rho_{is(j,2),k}^n - \rho_{is(j,1),k}^n\Big)\right] \\
&\quad + \Delta t\left[(K_{mv})_{j,k}\frac{u_{j,k+1}^{n+1} - u_{j,k}^{n+1}}{\Delta z_{j,k+1/2}^n}\right. \\
&\quad \left. -(K_{mv})_{j,k-1}\frac{u_{j,k}^{n+1} - u_{j,k-1}^{n+1}}{\Delta z_{j,k-1/2}^n}\right] \\
&\quad + \Delta z_{j,k}^n \Delta t \left\{\frac{\partial}{\partial x}\left[g\alpha\hat{\psi} - \frac{P_a}{\rho_0}\right]\right\}_{j,k}^n, \\
& j = 1,\ldots,N_s;\ k = m_j,\ldots,M_j, \quad (39)
\end{aligned}$$

where u is the normal velocity, and $u_{j,k}^*$ is the backtracked value at time step n at the foot of the characteristic line (see Section 3.4). All the right-hand side terms except for the elevation gradient and the vertical viscosity terms are treated fully explicitly. The discretized form of the tangential momentum equation is similar.

The discretized continuity and momentum equations can be written in compact matrix form as

$$\mathbf{A}_j^n U_j^{n+1} = \mathbf{G}_j^n - \theta\, g\frac{\Delta t}{\delta_j}\left[\eta_{is(j,2)}^{n+1} - \eta_{is(j,1)}^{n+1}\right]\Delta \mathbf{Z}_j^n \quad (40)$$

$$\mathbf{A}_j^n \mathbf{V}_j^{n+1} = \mathbf{F}_j^n - \theta g\frac{\Delta t}{l_j}\left[\hat{\eta}_{ip(j,2)}^{n+1} - \hat{\eta}_{ip(j,1)}^{n+1}\right]\Delta \mathbf{Z}_j^n \quad (41)$$

$$\begin{aligned}
\eta_i^{n+1} &= \eta_i^n - \frac{\theta\,\Delta t}{P_i}\sum_{l=1}^{i34(i)} s_{i,l}\ell_{jsj}\left[\Delta \mathbf{Z}_{jsj}^n\right]^{\mathrm{T}} \mathbf{U}_{jsj}^{n+1} \\
&\quad - \frac{(1-\theta)\Delta t}{P_i}\sum_{l=1}^{i34(i)} s_{i,l}\ell_{jsj}\left[\Delta \mathbf{Z}_{jsj}^n\right]^{\mathrm{T}} \mathbf{U}_{jsj}^{n}, \quad (42)
\end{aligned}$$

where $\mathbf{G}_j^n$ and $\mathbf{F}_j^n$ are vectors that combine all explicit terms (including the baroclinic forcing), and where

$$\mathbf{U}_j^{n+1} = \begin{bmatrix} u_{j,M_j}^{n+1} \\ \vdots \\ u_{j,m_j}^{n+1}\end{bmatrix}, \quad \mathbf{V}_j^{n+1} = \begin{bmatrix} v_{j,M_j}^{n+1} \\ \vdots \\ v_{j,m_j}^{n+1}\end{bmatrix}, \quad \Delta \mathbf{Z}_j^{n} = \begin{bmatrix} \Delta z_{j,M_j}^{n} \\ \vdots \\ \Delta z_{j,m_j}^{n}\end{bmatrix}. \quad (43)$$

Matrix $\mathbf{A}$, after adjustment to include the vertical boundary conditions (Eqs. (9) and (13)) and applicable horizontal boundary conditions, remains tri-diagonal, and thus can be inverted quite efficiently. Normal velocities can therefore be expressed as

$$\mathbf{U}_j^{n+1} = [\mathbf{A}_j^n]^{-1}\mathbf{G}_j^n - \theta g\frac{\Delta t}{\delta_j}\left[\eta_{is(j,2)}^{n+1} - \eta_{is(j,1)}^{n+1}\right][\mathbf{A}_j^n]^{-1}\Delta \mathbf{Z}_j^n \quad (44)$$

and substitution of Eq. (44) into (42) leads to a set of equations for elevations at all elements ($1 \leqslant i \leqslant N_e$):

$$\begin{aligned}
&\eta_i^{n+1} - \frac{g\theta^2\,\Delta t^2}{P_i}\sum_{l=1}^{i34(i)} \frac{s_{i,l} l_{jsj}}{\delta_{jsj}}\left[\Delta \mathbf{Z}_{jsj}^n\right]^{\mathrm{T}} \\
&\left[\mathbf{A}_{jsj}^n\right]^{-1}\Delta \mathbf{Z}_{jsj}^n\left[\eta_{is(jsj,2)}^{n+1} - \eta_{is(jsj,1)}^{n+1}\right] \\
&= \eta_i^n - \frac{(1-\theta)\Delta t}{P_i}\sum_{l=1}^{i34(i)} s_{i,l} l_{jsj}\left[\Delta \mathbf{Z}_{jsj}^n\right]^{T}\mathbf{U}_{jsj}^n \\
&- \frac{\theta\,\Delta t}{P_i}\sum_{l=1}^{3} s_{i,l} l_{jsj}\left[\Delta \mathbf{Z}_{jsj}^n\right]^{\mathrm{T}}\left[\mathbf{A}_{jsj}^n\right]^{-1}\mathbf{G}_{jsj}^n, \quad (45)
\end{aligned}$$

from which elevations can be solved. As indicated in Casulli and Zanolli (1998), the coefficient matrix resulting from the above system of equations is symmetric and positive definite, and thus efficient sparse matrix solvers like Jacobian Conjugate Gradient can be utilized.

At open boundaries, elevations may be specified, elevations may be nudged to specified values, or transmissive boundary types (e.g., Flather (1987)) may be applied. Because strict transmissive boundary conditions can be very involved for unstructured grids, a simplified form is used, where the open-boundary elevations are computed as the average over all adjacent non-open boundary elements, assuming that the phase speed there is equal to the average grid size divided by the time step.

Once the elevations are known, normal velocities can be computed at face centers by using Eq. (44). UnTRIM converts these normal velocities directly to the horizontal velocities at each node, using purely geometric arguments. However, we found this approach unsatisfactory in ELCIRC for benchmarks where Coriolis is a significant factor (e.g., Sections 4.2 and 4.4). Instead, we solve for the tangential momentum equation, Eq. (41), prior to mapping velocities at the nodes. Although more time consuming than UnTRIM's, this approach is still computationally efficient. Indeed, it fully reuses matrix A, as formed and inverted for the solution of the normal momentum equation.

Integral to the approach is, however, knowing elevations at nodes, $\hat{\eta}$, so that pressure gradients along sides can be computed. We estimate nodal elevations from elevations at element centers, computed earlier through Eq. (45), by using the formula

$$\hat{\eta}_i^{n+1} = \frac{\int \eta \, \mathrm{d}S}{\int \mathrm{d}S} = \frac{\sum_j P_{ine(i,j)} \eta^{n+1}_{ine(i,j)}}{\sum_j P_{ine(i,j)}}, \quad i = 1, \ldots, N_p, \tag{46}$$

where the integrations and summations are carried out over a "ball" around node i, with contributions from all surrounding elements, $ine(i,j)$. The formula can be argued to be algebraically consistent with volume conservation within the ball (not shown).

3.4. Backtracking and interpolation along characteristic lines

Both in the momentum equations (Section 3.3) and in the equations of salt and heat conservation (Section 3.6), we avoid usual Courant number constraints by incorporating advection in total derivatives, and solving the resulting equations in an Eulerian–Lagrangian context. Integral to this approach is the ability to backtrack characteristic lines efficiently and accurately (e.g., see Oliveira and Baptista, 1998), starting from known locations at time $n+1$. Once the location of the foot of the characteristic lines at time n is found, initial conditions at that time step can be obtained for the variable of interest by either interpolation or integration (Oliveira and Baptista, 1995).

In practice, backtracking is the single most time-consuming part of our solution, a problem that is aggravated by the fact that we backtrack twice: first for the momentum equation, and then—using updated flow fields and a larger set of characteristic lines—again for the scalar-transport equations. Backtracking for momentum starts always at side centers, while backtracking for salinity and temperature starts both at side centers and nodes (see Section 3.6). The approach is the same, regardless of location. In all cases, backtracking requires the 3D solution, backwards from $n+1$ to n, of

$$\frac{\mathrm{d}x_i}{\mathrm{d}t} = u_i^m(x_1, x_2, x_3, t) \quad \text{with} \quad i = 1, 2, 3, \tag{47}$$

where m either stands for time step n (for momentum) or denotes a linear interpolant between $n+1$ and n (for salinity and temperature). Hence, flow fields are always known beforehand.

As a compromise between accuracy and computational efficiency, we backtrack using a simple Euler integration of Eq. (47), but with a time step smaller than Δt. The approach is illustrated in Fig. 4, and represents a deviation from more elaborated strategies that we have used in 2D models such as Baptista et al. (1984), Oliveira and Baptista (1995), Wood et al. (1995) and Oliveira et al. (2000). The reader is referred to Oliveira and Baptista (1998) for an analysis on how tracking errors may destroy the positivity and mass conservation of solutions of the transport equation.

Also, in a deviation from our prior models, we chose linear interpolation at the feet of the characteristic lines for both momentum and scalar-transport equations. The defining advantage of linear interpolation is the positivity[5] of the solutions, a property that we found particularly important in addressing the representation of

[5]Positivity requires that solutions remain bounded by the initial maxima and minima, in the absence of external sources and sinks (and, thus, implies the absence of numerical oscillations).

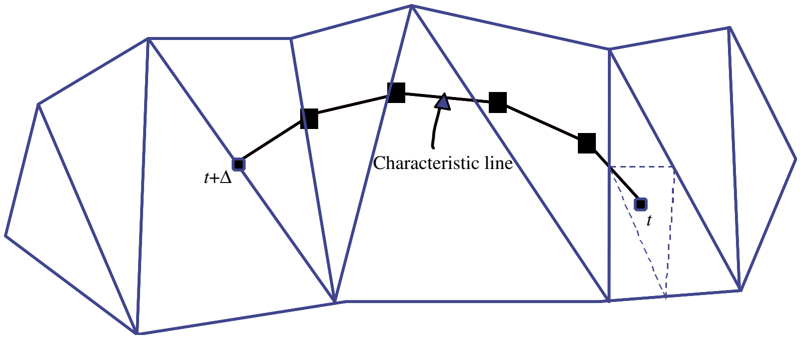

Fig. 4. Backtracking of the characteristic lines (illustrated here in a 2D setting) is a time-consuming operation. It involves, for each "origin" at time $t+\Delta t$, the 3D solution of Eq. (47). A simple Euler method is employed, but multiple tracking sub-steps are allowed within the overall time step Δt. The number of sub-steps is imposed by the user, but might be overridden by code-controlled adjustments accounting for local flow gradients.

baroclinic forcings (e.g., see discussion in Section 3.6). The disadvantage is that linear interpolation introduces numerical diffusion (Baptista (1987); also, Section 4.1.3). To reduce numerical diffusion in the solution of the salinity and temperature, we sub-split (Fig. 3c) the original grid elements into four before interpolating (which is the reason why we solve the salt and heat balance equations at both nodes and side centers). We do not use splitting to solve the momentum equations, where advection terms—albeit important—often do not have as dominant a role; should the need arise, the horizontal grid must thus be refined to reduce numerical diffusion.

3.5. Vertical velocity solution

Defined as a constant within each element, the vertical velocity can be calculated from the 3D continuity equation through a finite-volume approach:

$$w_{i,k}^{n+1} = w_{i,k-1}^{n+1} - \frac{1}{P_i}\sum_{j=1}^{i34(i)} s_{i,j} l_{jsj} \Delta z_{jsj,k}^{n} u_{jsj,k}^{n+1},$$

$$k = m_i^e, \ldots, M_i^e \qquad (48)$$

Although only the bottom boundary condition $w_{i,m_i^e-1}^{n+1} = 0$ is needed in this recursive formula, due to volume conservation the free-surface condition is also automatically satisfied, within a very small closure error. This is expected because Eq. (2) is derived by integrating Eq. (1) over depth with kinematic boundary conditions at the bottom and free surface (cf., Luettich et al., 2002).

While much smaller in magnitude than the horizontal velocities, the vertical velocity strongly affects the stability of stratification in estuaries and plumes. In our experience in the Columbia River estuary, overestimation or parasitic oscillations in the computation of vertical velocities can easily transform a two-layer flow into a well-mixed flow. Because the vertical velocity is a measure of the horizontal divergence, this effectively means that there is very little tolerance for numerical oscillations on the horizontal velocities. A practical consequence is that, for strongly stratified flows, time steps must be selected consistently with the celerity of internal baroclinic waves (see also Section 3.6).

3.6. Solving for salt and heat balances

The numerical solution for salinities and temperature is obtained in an Eulerian–Lagrangian framework by the finite-difference solution of Eq. (5) or (6), at both nodes or side centers. An example is given below, for the solution of salinity at a side center:

$$\Delta z_{i,k}^{n}\left(S_{i,k}^{n+1}-S_{i,k}^{*}\right)=\Delta t\left[(K_{hv})_{i,k}\frac{S_{i,k+1}^{n+1}-S_{i,k}^{n+1}}{\Delta z_{i,k+1/2}^{n}}-(K_{hv})_{i,k-1}\frac{S_{i,k}^{n+1}-S_{i,k-1}^{n+1}}{\Delta z_{i,k-1/2}^{n}}\right]$$
$$(i=1,\ldots,N_s,k=m_i,\ldots,M_i), \quad (49)$$

where S is defined at half levels and $S_{i,k}^{*}$ is the value at the foot of the characteristic lines. Very similar equations result for temperature, and for solutions at nodes rather than side centers.

After backtracking and local interpolation, temperature and salinity are solved independently at each vertical (node or side center) via Eq. (49) or similar. In addition, Neuman-type boundary conditions are imposed at both the bottom and free surface, consistently with Section 2.3.3. Horizontally, the salinity and temperature at open boundaries are most often specified during inflow and radiated freely during outflow (which the backtracking allows for rather naturally).

We note that the continuity and momentum equations are coupled to the salt and heat balance equations via the baroclinic pressure term. This term, if treated improperly, can in strongly stratified regions (e.g. the Columbia River estuary) create noise in the horizontal flow field, leading to noise in the vertical velocity field, with the potential to quickly annihilate stratification. Keys to successfully handling baroclinic forcing appear to be (a) the use of time steps limited by the speed of propagation of internal baroclinic waves, rather than of barotropic waves; and (b) positivity-preserving strategies for transported quantities (Section 3.4).

It is also important to avoid underestimating baroclinic effects by overly diffusing the density field. Numerical diffusion in salt and temperature transport can be controlled by: using time steps that lead to Courant numbers larger than unity, thus reducing the number of required interpolations (cf., Eq. (55), Section 4.1.3); and enabling sufficient spatial resolution (including sub-splitting, Section 3.4) to resolve physically important gradients.

3.7. Parameterizing turbulence

The momentum and transport equations contain vertical viscosity and diffusivity that must be parameterized (Section 2.4). While no additional equations must be solved with zero-equation closures, both GLS and MY25 require two additional transport equations. We consider here the case of GLS. The turbulent kinetic energy and mixing length are both defined at side centers and at half levels, and the approach to solving the two closure equations is similar to that for the scalar-transport equations (e.g., Eq. (49)). However, advection is neglected, and therefore no backtracking is involved: the resulting equation is directly 1D in the vertical direction.

Following Warner et al. (2004), we enhance numerical stability through two procedures. First, the production terms are treated either explicitly or implicitly depending on the sign. For example, the equation for the generic length-scale variable ψ, Eq. (22), is discretized as

$$\Delta z_{j,k}^{n}(\psi_{j,k}^{n+1}-\psi_{j,k}^{n})=\Delta t\left[(v_\psi)_{j,k}^{n}\frac{\psi_{j,k+1}^{n+1}-\psi_{j,k}^{n+1}}{\Delta z_{j,k+1/2}^{n}}-(v_\psi)_{j,k-1}^{n}\frac{\psi_{j,k}^{n+1}-\psi_{j,k-1}^{n+1}}{\Delta z_{j,k-1/2}^{n}}\right]+M-\Delta t\,\Delta z_{j,k}^{n}c_{\psi 2}[F_w(c_\mu^0)^3k^{1/2}\ell^{-1}]_{j,k}^{n}\psi_{j,k}^{n+1},$$
$$j=1,\ldots,N_s,k=m_j,\ldots,M_j, \quad (50)$$

where the production term is treated as:

$$M=\begin{cases}\Delta t\,\Delta z_{j,k}^{n}(c_{\psi 1}K_{mv}M^2+c_{\psi 3}K_{hv}N^2)_{j,k}^{n}\frac{\psi_{j,k}^{n+1}}{k_{j,k}^{n}}, & \text{if } M\leqslant 0,\\ \Delta t\,\Delta z_{j,k}^{n}(c_{\psi 1}K_{mv}M^2+c_{\psi 3}K_{hv}N^2)_{j,k}^{n}\frac{\psi_{j,k}^{n}}{k_{j,k}^{n}}, & \text{if } M>0.\end{cases} \quad (51)$$

Secondly, the boundary conditions for the two GLS equations are recast into flux form:

$$v_k^{\psi}\frac{\partial k}{\partial z}=0, \quad \text{at} \quad z=H_R-h \quad \text{or} \quad z=H_R+\eta, \quad (52)$$

$$v_\psi\frac{\partial\psi}{\partial z}=\kappa n v_\psi\frac{\psi}{\ell}, \quad \text{at} \quad z=H_R-h, \quad (53)$$

$$v_\psi \frac{\partial \psi}{\partial z} = -\kappa n v_\psi \frac{\psi}{\ell}, \quad \text{at} \quad z = H_R + \eta. \tag{54}$$

Only after k and ψ are found with the above boundary conditions, are the original boundary conditions, Eqs. (32) and (33), enforced.

3.8. Solving for wetting and drying

One of the major advantages of the formulations of Casulli and Cheng (1992) and of Casulli and Zanolli (1998) is their natural and robust handling of wetting and drying. We retain their approach in ELCIRC, in what amounts to primarily careful bookkeeping of indices. After all unknowns have been found for time step $n+1$, the free-surface indices are updated with the newly computed elevations. Elements are dried if $h+\eta<h_0$ (a small positive number, h_0, is used in the code in lieu of zero in order to avoid underflow). It is also noteworthy that in the limit of only one vertical layer, the above formulation and numerics automatically reduce to the 2D depth-integrated version.

4. Numerical benchmarks

Controlled numerical benchmarks have been very useful in understanding and enhancing ELCIRC. A sub-set of these benchmarks is described below, organized under four themes: basic numerical properties, Coriolis representation, representation of stratification, and representation of qualitative plume behavior.

4.1. Basic numerical properties

Similarly to TRIM and UnTRIM, the underlying numerical algorithm of ELCIRC is well adapted to large Courant numbers, and is volume conserving, positivity preserving, low order, and numerically diffusive (cf., Eq. (55)). The reader is referred to Casulli and Cattani (1994) for contextual formal analysis of the stability and accuracy of this type of method. Also useful is the extensive body of literature available on Eulerian–Lagrangian methods for scalar transport, including Baptista (1987), Oliveira and Baptista (1995), Oliveira and Baptista (1998), and Oliveira et al. (2000). In the following subsections, we use simple benchmarks to illustrate the key numerical properties of ELCIRC. Further details on these and other benchmarks, including input files to reproduce benchmark results, are available electronically (CCALMR, 2003).

4.1.1. Volume conservation

Volume conservation is algorithmically enforced through the use of a finite-volume strategy. In practice, the testing of early versions of ELCIRC revealed that substantial deviations from strict volume conservation might result from ambiguity in coding choices on the treatment of inter-element discontinuities and wetting and drying. However, attention to coding detail can virtually eliminate volume conservation errors. New versions of ELCIRC are now tested for volume conservation through a benchmark that involves moving a fixed discharge along an irregular riverbed, with both horizontal and vertical complexity (Fig. 5a). This benchmark is inspired on the need of cross-scale models to correctly propagate freshwater volumes and rates through river networks to estuaries and ultimately the ocean. The desired result of the benchmark is to exactly match inflow and outflow discharges, at equilibrium. As illustrated in Fig. 5b, ELCIRC_v5.01 inflow and outflow discharges at control transects do indeed match. Numerically, the match is within 0.002% of the equilibrium discharge.

4.1.2. Implictness factor

Casulli and Cattani (1994) and Casulli and Zanolli (1998) showed that the judicious choice of implicit or explicit treatment for each term of the momentum equation is critical for the computational performance, algorithmic robustness and accuracy of TRIM and UnTRIM (cf., Section 3.1). Casulli and Cattani (1994) further suggest a significant effect of the choice of the implicitness factor, θ, used for terms being treated semi-implicitly. In particular, stability requires $0.5\leqslant\theta\leqslant 1$, and theoretical optimal accuracy is obtained for $\theta=0.5$, with numerical damping increasing progressively for larger θ. While these

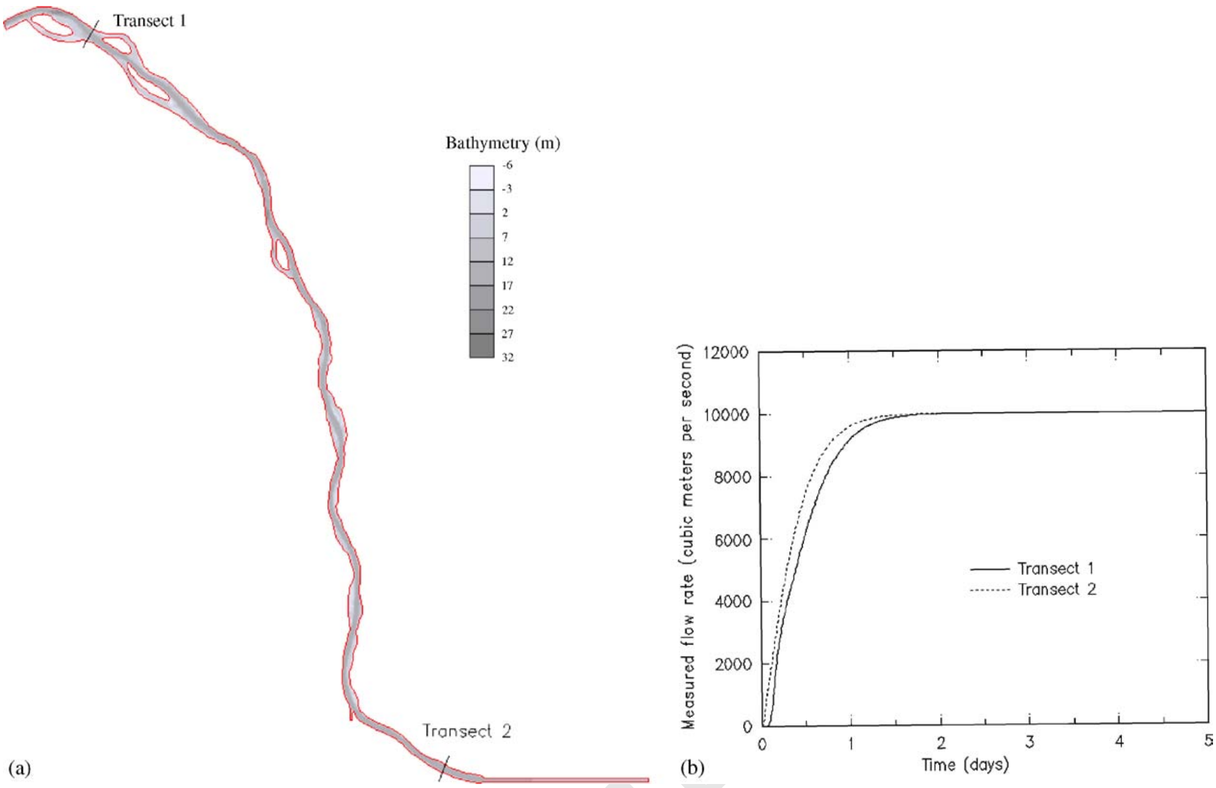

Fig. 5. Volume conservation of successive ELCIRC implementations is systematically tested against the irregular riverine domain shown in (a). Discharges are measured at control cross sections (transects 1 and 2). For several versions now ELCIRC results have been consistently very good. Results for ELCIRC_v5.01 are shown in (b).

guidelines are strictly valid only under idealized conditions, they tend to be broadly useful.

Here, we use a conventional benchmark to examine the role of θ on ELCIRC accuracy for depth-averaged long-wave propagation over a linearly sloping bottom. The computational domain is a quarter annulus with inner and outer radii of 60,960 and 152,400 m (Fig. 6a). Water depths at the inner (land) and outer (ocean) boundaries are 10.02 and 25.05 m, respectively. An M_2 tide of amplitude 0.3048 m propagates from the open ocean to the slope and is refracted and reflected by the bottom and land boundaries. Water is considered inviscid, and the bottom frictionless. Assuming linearity (a reasonable approximation, given the choice of water depths and tidal amplitudes), an exact solution exists for the problem (Lynch and Gray, 1978).

A convergence study, using several horizontal grids, time steps and implicitness factors showed that large time steps (and Courant numbers well above unity) may be used in ELCIRC for this barotropic problem without incurring instability, provided $0.5 \leqslant \theta \leqslant 1$. Results are presented in Fig. 6b for $\Delta t = 1047.93$ s, and show the behavior of error relative to the implicitness factor. Error metrics shown are percentage errors relative to the analytical solution of the amplitude of M_2 elevations and radial velocities, at a node located 240 m from the inner boundary. Only the stability region is shown. As anticipated by the analysis of Casulli and Cattani (1994), accuracy degrades

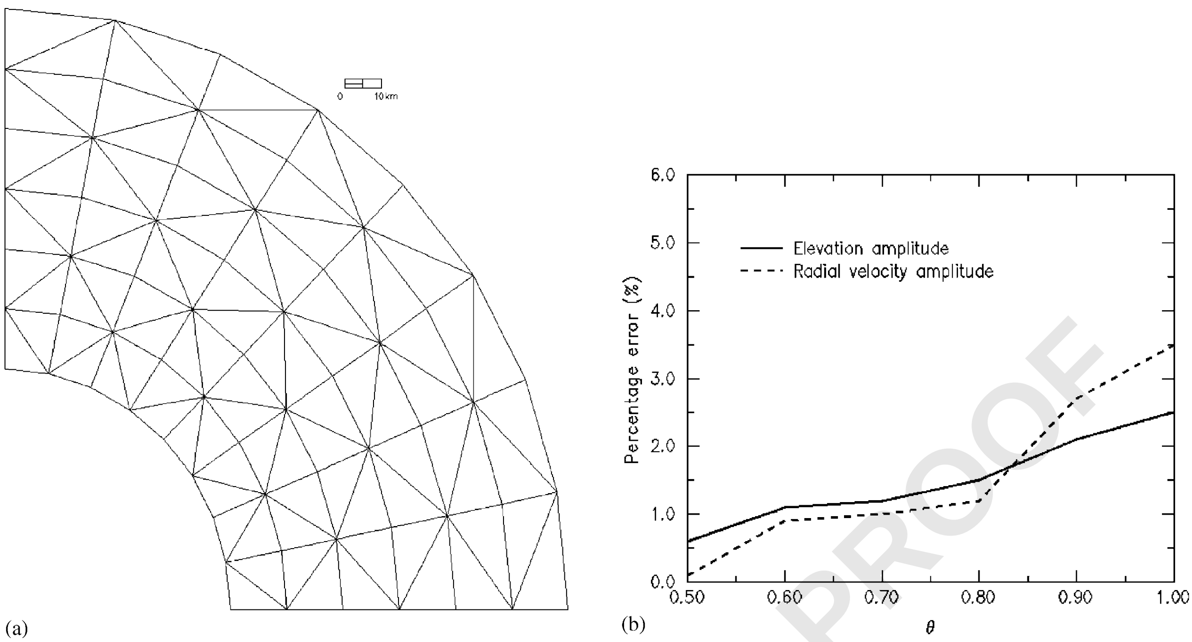

Fig. 6. Long-wave propagation over a linearly sloping bottom. The horizontal discretization of the quarter annulus domain is shown in (a). The problem is solved for a single vertical layer. Results, shown in (b) in the form of percentage errors for the amplitudes of M2 elevation and radial velocity, illustrate that accuracy degrades progressively with the increase of the implicitness factor within the stability region ($0.5 \leqslant \theta \leqslant 1$).

progressively from $\theta = 0.5$ to 1, reflecting increasing numerical damping.

In practice, we often adopt $\theta = 0.6$ to remain close to optimal accuracy while eliminating or minimizing any oscillations introduced by the baroclinic terms not included in the analysis of Casulli and Cattani (1994).

4.1.3. Transport in an uniform flow

Eulerian–Lagrangian solutions of the transport equation have been extensively studied in the literature and are commonly used in scientific and engineering applications. The single largest advantage of this class of methods is their ability to handle Courant numbers larger than unity. Yet, solutions are not strictly mass preserving (Oliveira et al., 2000), require accurate tracking of characteristic lines as a pre-condition for overall accuracy and mass conservation (Oliveira and Baptista, 1998), and may exhibit substantial numerical diffusion depending on the choice of the interpolation or integration approach used at the foot of the characteristic lines (Baptista, 1987; Oliveira and Baptista, 1995). As discussed earlier, we chose to implement in ELCIRC an adjustably accurate tracking algorithm for characteristic lines, to enable control over positivity preservation and mass conservation. Also, we use simple linear interpolation at the foot of the characteristic lines, a choice driven by efficiency and positivity considerations but known to induce numerical diffusion—thus placing on the user the onus of choosing an appropriate time step and spatial resolution. To partially mitigate numerical diffusion, ELCIRC splits—during the solution of the scalar-transport equations—each element of the numerical grid into four sub-elements (Fig. 3c), which increases the dimensionless wavelength of the transported fields.

In this section, we use the conventional problem of advective transport of a scalar field in a uniform flow, to show that ELCIRC follows expected behavior relative to the theory of Eulerian–Lagrangian methods. The reference simulation consists of advecting a Gauss hill, with standard deviation 1 km and amplitude 5 °C (above a background temperature of 5 °C), in a flow field constant in space and time with $u = 0.1\,\mathrm{m}^{-1}\,\mathrm{s}$ and $v = 0$. The problem was set up computationally with a $30\,\mathrm{km} \times 6\,\mathrm{km}$ rectangular channel of constant depth 20 m, which was then uniformly meshed with quadrangles with $\Delta x = \Delta y = 250\,\mathrm{m}$. The correct solution is the transport of the Gauss hill by the ambient flow without any deformation. The problem is essentially 1D in the x-direction. We can formally show that in this case the ELCIRC algorithm has a diffusion-like leading-order truncation error, of the form

$$\varepsilon = \frac{f''_*}{8}\Delta x^2 \mathit{frac}(Cu)(1 - \mathit{frac}(Cu)), \qquad (55)$$

where $Cu = 2u\Delta t/\Delta x$ is the Courant number (defined to account for the splitting in sub-elements), $\mathit{frac}(Cu)$ is the fractional part of the Courant number, and f''_* is the second derivative of the solution at the foot of the characteristic line.

Fig. 7 synthesizes results of several ELCIRC simulations. Fig. 7a shows that errors per time step mimic the behavior predicted by Eq. (55). Fig. 7b illustrates the diffusive nature of the underlying algorithm, and shows that the use of larger time steps improves accuracy after a set period of time. This latter trend is common in Eulerian–Lagrangian methods, the explanation being that errors per time step depend on $\mathit{frac}(Cu)$ rather than Cu, and thus larger time steps imply less instances of a similar error over a fixed period of time. Note that, in spite of this trend, Eulerian–Lagrangian methods are numerically consistent, with the truncation errors approaching zero when both Δx and Δt tend to zero (Baptista, 1987). Finally, Fig. 7c is a reminder that the method is only first order in space.

4.2. *Coriolis representation*

Coriolis plays a major role in coastal dynamics, and its correct representation is a critical requirement for cross-scale, river-to-ocean circulation models. While early versions of ELCIRC were unable to meet this requirement, the problem was overcome by the inclusion of the momentum equation for the transversal velocities (Section 3.3), one of the significant deviations of ELCIRC relative to UnTRIM. We present below results of ELCIRC_v5.01 for two benchmarks that were instrumental in identifying and remedying the initial problems.

4.2.1. *Geostrophic flow in a straight channel*

In the presence of Coriolis, flow in a constrained channel develops a lateral slope normal to the mean flow direction. A steady-state analytical solution for an inviscid fluid can be found by balancing the pressure gradient with Coriolis (Pond and Pickard, 1998). Matching this analytical solution requires correct representation of Coriolis. We consider here a $20\,\mathrm{km} \times 1\,\mathrm{km}$ rectangular channel of constant depth 20 m, with the right end linked to a large deep basin ($20\,\mathrm{km} \times 5\,\mathrm{km} \times 200\,\mathrm{m}$) to reduce downstream boundary effects. We place the channel at 45°N latitude (i.e., $f \approx 10^{-4}\,\mathrm{s}^{-1}$), and impose a constant flow of $1.98 \times 10^4\,\mathrm{m}^3\,\mathrm{s}^{-1}$ on the left end of the channel. Surface elevations on the basin end are kept at MSL. Both a uniform triangular grid ($\Delta x = 125\,\mathrm{m}$; $\Delta y = 2\,\mathrm{km}$) and moderate non-uniform variations thereof were tested, with essentially identical results. The vertical resolution Δz varies from 5 to 100 m, and the time step is set at 5 min. A steady state is established shortly after a 1-day ramp-up. Away from the boundary, the flow is essentially uniform inside the channel (Fig. 8a, b), with a maximum error in the computed velocity of about 1 cm/s (or 1% of the theoretical velocity of $1\,\mathrm{m\,s}^{-1}$). A nearly linear elevation slope is established normal to the flow, and compares well with the analytical solution (Fig. 8c).

4.2.2. *Ekman dynamics*

Away from the equator, wind blowing over the ocean leads to circulation patterns of major oceanographic and ecological relevance. *Ekman dynamics* (e.g., see Pond and Pickard, 1998) describes the expected behavior for a steady wind blowing over an infinitely deep and wide ocean with constant density, assuming a balance between friction (wind stress and vertical eddy viscosity) and Coriolis. The analytical solution shows currents at an angle with the direction of the

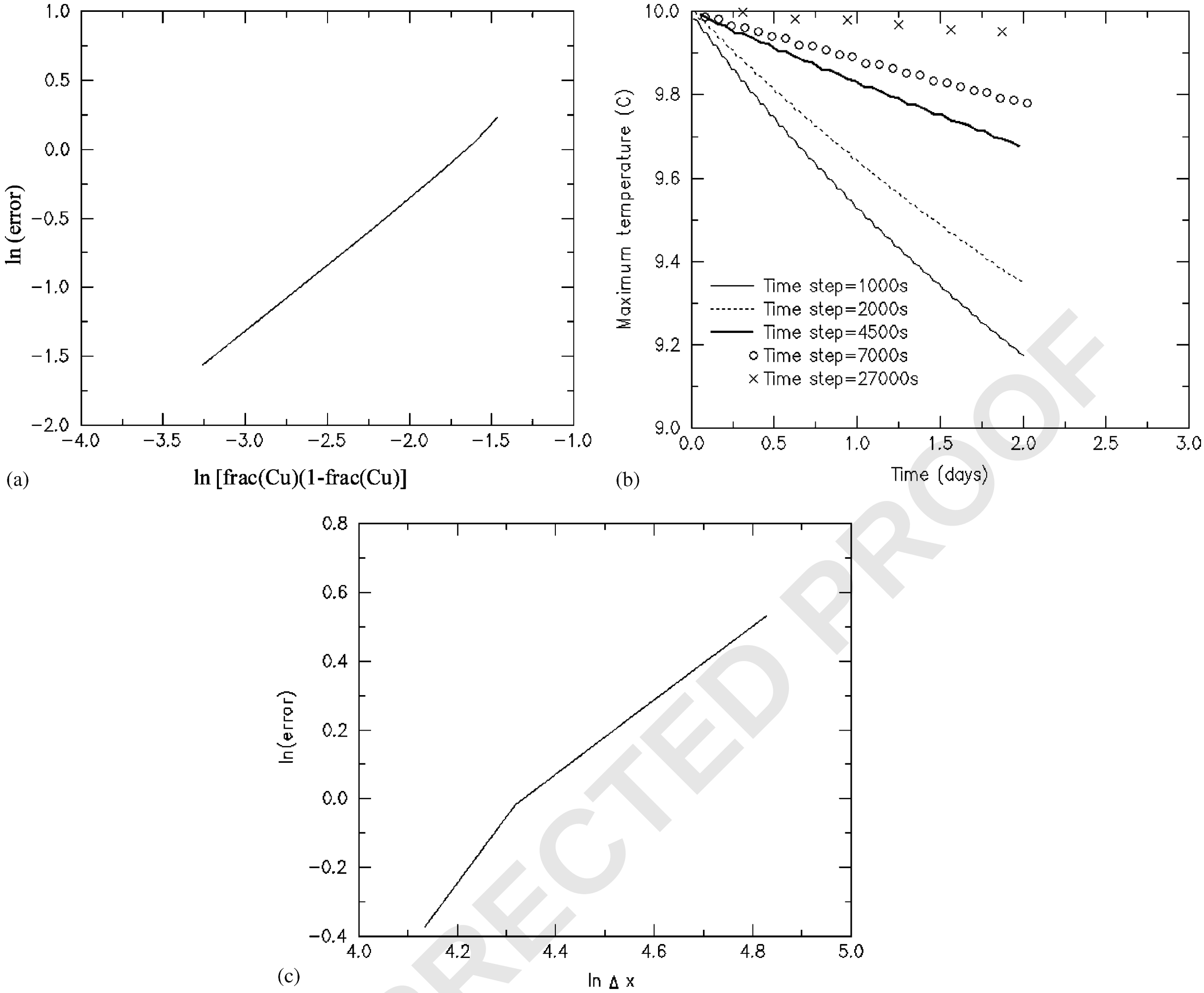

Fig. 7. Advection of a Gauss Hill in an uniform flow. (a) Errors per time step depend on the fractional part of the Courant number, as anticipated by Eq. (55). Results shown are for a fixed $\Delta x = 250\,\mathrm{m}$, and variable Δt. (b) Numerical damping at a fixed time increases with decreasing time step. Results shown are for a fixed $\Delta x = 250\,\mathrm{m}$. (c) Errors as a function of Δx, showing first-order convergence. Results shown are for a fixed $\Delta t = 500\,\mathrm{s}$.

wind: 45° to the right of the wind direction at the surface, in the northern hemisphere, and rotating with depth in a spiral pattern known as the *Ekman spiral*. At the *Ekman depth*, the direction of the wind-driven current is exactly opposite to its direction at the surface. The velocity of *Ekman currents* decays exponentially with depth, from about 1.5% of the wind speed at the sea surface to 0.06% at the Ekman depth.

We describe in this section ELCIRC_5.01 solutions for an Ekman dynamics benchmark problem. We consider a square domain of $100\,\mathrm{km} \times 100\,\mathrm{km}$ with a flat (50 m in depth) and frictionless bottom (to approximate an infinite depth) at about 45°N latitude ($f \approx 10^{-4}\,\mathrm{s}^{-1}$). The uniform wind is set at $10\,\mathrm{m\,s}^{-1}$, and the constant vertical eddy viscosity at $10^{-4}\,\mathrm{m}^2\,\mathrm{s}^{-1}$. The horizontal resolution is uniform with $\Delta x = \Delta y = 2\,\mathrm{km}$, and Δz varies from 0.5 at the surface to

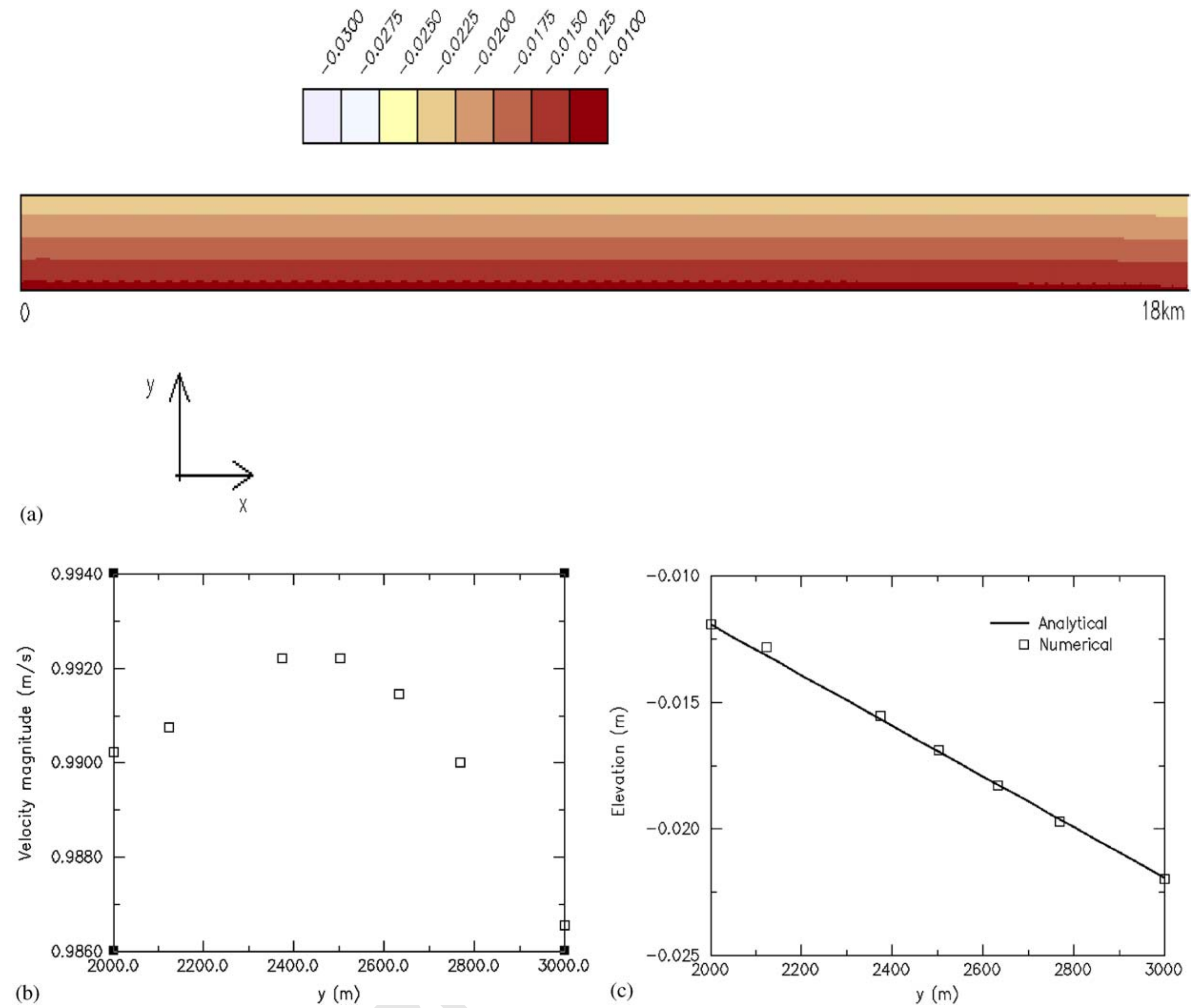

Fig. 8. Geostrophic flow in a straight channel, for a uniform grid. (a) Isolines of elevation after 5 days. (b) Cross-sectional velocity magnitudes, at $x = 10$ km (exact solution is $1\,\mathrm{m\,s^{-1}}$). (c) Comparison of analytical and numerical solutions for elevation at $x = 10$ km.

27 m at the bottom (we have also conducted tests with moderately non-uniform grid variations, with essentially the same results). The elevation is clamped at the MSL on the four edges of the square domain. The time step is set at 5 min. The non-linear advection terms are turned off to facilitate comparison with the analytical solution. To study the sensitivity of the solution with respect to the wind direction, we applied two wind directions of 90° ("North") and 60° to the horizontal.

A quasi-steady state, with small inertial perturbations, is established shortly after the ramp-up period (which is 1 day in this case), with uniform velocity at each layer (except for slight variations near the boundary). Other than a rigid-body rotation, the solution is not sensitive to the choice of wind direction, thus suggesting the correct treatment of Coriolis in the numerical scheme. The vertical profiles of velocity at the center of the domain, averaged over 3 days after ramp-up, are compared with the analytical solution (Fig. 9a–d). The comparison is generally excellent inside the

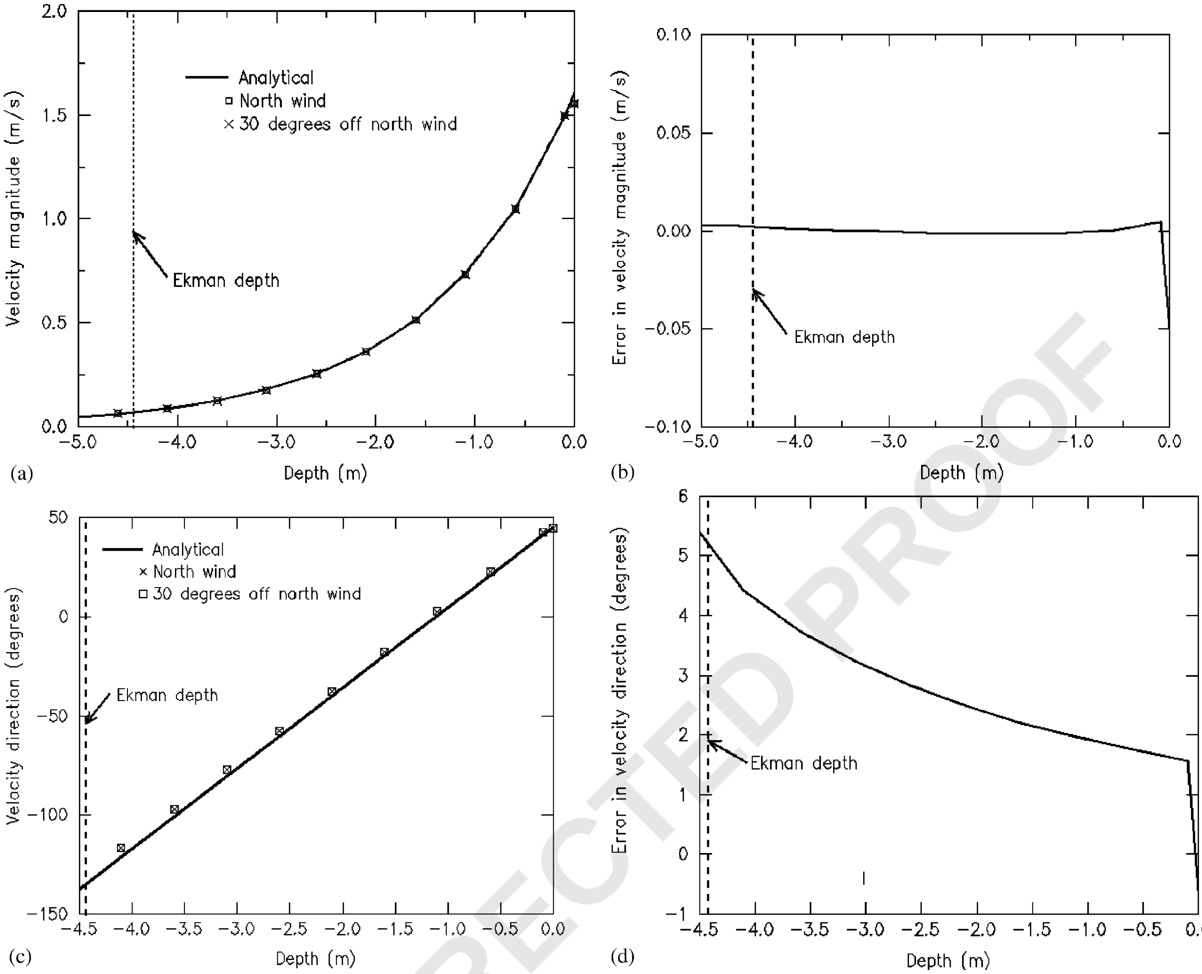

Fig. 9. Ekman dynamics. Comparison of analytical and steady-state ELCIRC solutions at the center of a square domain, under alternative wind directions. (a) Velocity magnitude. (b) Error in velocity magnitude. (c) Velocity direction. (d) Error in velocity direction.

Ekman layer (below the Ekman depth the velocity is very small and the comparison between the numerical and analytical solutions has no practical significance). Errors increase right at the surface of the Ekman layer, an artifact of the representation of normal and tangential velocities at half levels (rather than exactly at the surface).

4.3. Adjustment under gravity

Stratification plays an important role in the dynamics of estuarine and marine systems. A demanding benchmark for the ability of circulation models to represent stratification involves the gravitational adjustment of two fluids of different density, initially separated by a vertical wall (Wang, 1984). Once the vertical wall is removed, the fluids adjust through two density fronts traveling in opposite directions, to eventually form a stably stratified two-layer flow. While there is no strict analytical solution for this problem, models such as ROMS and SEOM have been extensively tested against it, with simulations evaluated both relative to qualitative behavior (e.g., front sharpness and solution smoothness) and quantitative metrics (celerity of propagation of density fronts; and maximum and minimum density).

The ELCIRC_v5.01 solution of the inviscid form of this problem is shown in Fig. 10a, with discretization and parameter choices described in the caption. Associated quantitative metrics show that the expected maxima and minima of density are exactly preserved—a consequence of positivity—but that the speed of the gravitational adjustment is about 84% of that predicted by linear theory. Increasing the vertical grid resolution by a factor of 4 increases the numerical celerity to 88% of the linear theory value.

Using two-and-a-half equation turbulent closures to characterize vertical mixing slightly reduces the sharpness of the solution, but does not substantially change the celerity of the adjustment, and does not destroy positivity. All GLS closures represented in ELCIRC_v5.01 provide nearly indistinguishable results, shown in Fig. 10b for $k-k\ell$. Results for MY25 (not shown) are similar. This similarity should not be extrapolated to more complex problems, as shown elsewhere (Baptista et al., 2004).

4.4. Qualitative plume behavior

Large freshwater plumes are dramatic and important oceanographic features, for which representation numerical models must be able to preserve the dynamic balance between inertia, vertical mixing, stratification and Coriolis. A particularly demanding benchmark involves the simulation of the plume resulting from a freshwater discharge in a quiescent ocean, under strong Coriolis (e.g., at a mid-latitude). While no analytical solution exists, key features of the expected behavior include anti-cyclonic turning of the plume outside the river mouth, development of a narrow coastal jet in the direction of Kelvin waves, very limited penetration on the opposite ("upstream") direction, and surface trapping of the plume.

We consider here the same forcings, physics and computational domain used by Garcia-Berdeal et al. (2002) to solve this benchmark with ECOM3D, a POM derivative. The settings are loosely inspired by typical winter conditions for the Columbia River plume. The domain consists of a deep rectangular "ocean" basin (140 km × 400 km), with a linearly sloping bottom (20 m depth at the coast and 300 m at the offshore boundary). Joining the "ocean" at 120 km north of the south boundary is an estuary of size 10 km × 4 km with a constant depth of 20 m. At the upstream river boundary, freshwater is steadily discharged into the top 10 m of the vertical column at a constant rate of 7000 $m^3 s^{-1}$. The south, west and north sides of the "ocean" are open. Coriolis is set at $f = 10^{-4} s^{-1}$. The simulation is cold started with a 1-day ramp-up. Vertical mixing is represented with MY25, with background viscosity and diffusivity of $10^{-6} m^2 s^{-1}$. We also adopted the horizontal

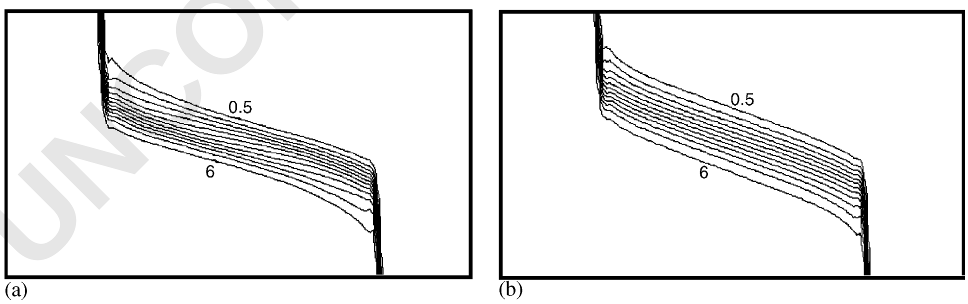

Fig. 10. Adjustment under gravity of two fluids of different densities, initially separated by a vertical "wall". Solutions were obtained in a 64 km × 20 km × 20 m domain, with $\Delta x = \Delta y = 500$ m, $\Delta z = 1$ m, and $\Delta t = 300$ s. No bottom friction or Coriolis were applied. Background temperature was uniformly set at 4 °C. Initial salinity was imposed as $S = (6.25/2)[1 - \tanh[(x - 32,000)/1000]],$, thus allowing for a sharp but continuous transition between 6.25 and 0 psu, respectively, to the left and right of the initial "wall". Results after 12 h, in the form of isolines every 0.5 psu, are shown for (a) inviscid laminar conditions, and (b) for a $k-k\ell$ closure.

discretization of Garcia-Berdeal et al. (2002), with a quadrangular grid with $\Delta x = 1.5$ km and $\Delta y = 2$ km. However, the differences between ECOM3D and ELCIRC require different strategies for the vertical discretization: rather than σ-coordinates, we used 43 z-levels with Δz varying from 0.5 to 117 m. We used $\Delta t = 5$ min.

Surface salinities at the end of a 14-day simulation are depicted in Fig. 11, and show a very good qualitative match both with expected key features and with the results of Garcia-Berdeal et al. (2002). This suggests that ELCIRC_v5.01 has the potential to represent, individually and in overall balance, the relevant physical processes involved in the description of complex plume behavior.

5. Concluding remarks

This paper presents the formulation and basic skill assessment of ELCIRC, an open-source numerical model for cross-scale simulation of river-to-ocean 3D circulation. A member by conceptual affinity, although not by implementation, of the class of finite volume Eulerian–Lagrangian models introduced by Casulli and Cheng (1992) and Casulli and Zanolli (1998), ELCIRC fills a void by opening such class of models to broad community use and feedback.

ELCIRC is a low-order model, which requires highly resolved horizontal and vertical grids, but enables large time steps (with Courant numbers in excess of unity) and appears capable of addressing a large variety of riverine and marine processes. The low-order and Eulerian–lagrangian nature of solution strategies in ELCIRC are in dramatic contrast with those of community models such as ADCIRC, QUODDY, POM, ROMS and SEOM, thus providing a truly distinctive alternative.

The Columbia River system, with its diverse challenges and tightly coupled scales and processes, provides an example of an application extremely well suited to a model like ELCIRC. Indeed, ELCIRC is now at the core of the circulation modeling system that we have been developing for the Columbia River, and supports semi-operational generation of multi-year simulations and routine daily forecasts of 3D baroclinic estuarine and plume circulation (Baptista et al., 2004).

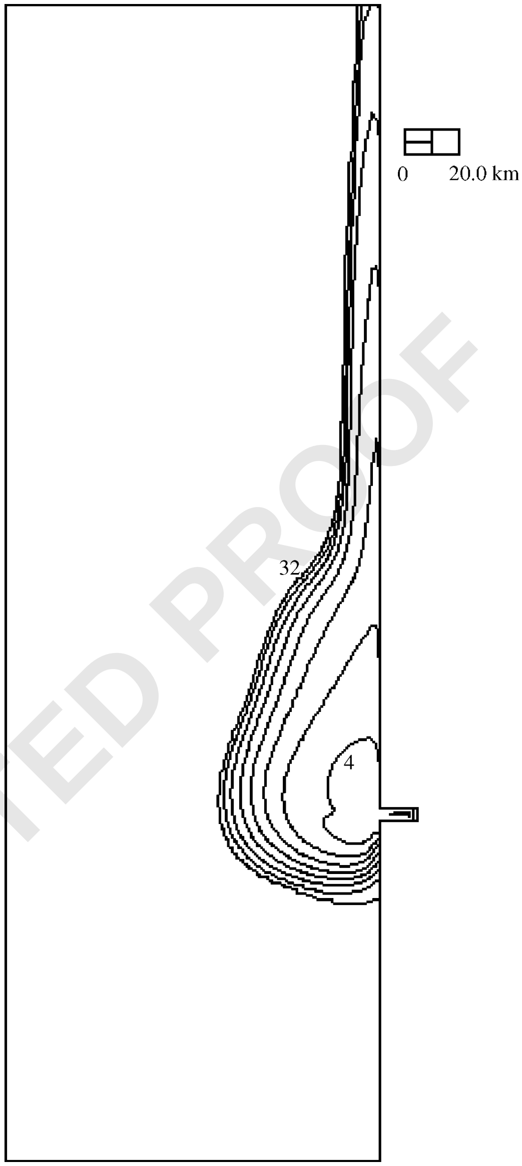

Fig. 11. Idealized plume under mid-latitude, Northern hemisphere Coriolis. Results are shown after 14 days, in the form of isolines of salinity at 4 psu increments. Simulations represent expected plume characteristics: anti-cyclonic turning outside the river mouth, development of a narrow coastal jet in the northern direction, very limited penetration of freshwater southwards, and (not shown) surface trapping.

However, ELCIRC is still an emerging model. On-going developments and other desirable efforts include formulation and algorithm alternatives, MPI-based parallelization in distributed-memory computer clusters, and extension to ecological processes. Priority formulation and algorithm alternatives include a non-hydrostatic formulation; a fully conservative, higher-order solution of scalar transports; and vertically stretched coordinates.

Acknowledgements

The development and testing of ELCIRC has greatly benefited from the contributions of many colleagues. Through both his published work and informal conversations with the second author in workshops in Denver and Delft, Prof. Vincenzo Casulli provided the conceptual foundation on which we built ELCIRC. Within the CORIE team, we are particularly grateful to Dr. Mike Zulauf for developing air–water exchange modules (see Appendix A); Dr. Arun Chawla for extended discussions on formulation and simulation quality; and Mr. Paul Turner for the creation of supporting pre- and post-processing tools. We are also grateful to Dr. Edmundo Casillas, of the National Oceanic and Atmospheric Administration (NOAA), for providing the driving application and partially facilitating the funded development of ELCIRC. ELCIRC has been developed through a combination projects funded by NOAA and the Bonneville Power Administration (NA17FE1486, NA17FE1026, NA87FE0405), the US Fish and Wildlife Service (133101J104), the Office of Naval Research (N00014-00-1-0301, N00014-99-1-0051), and the National Science Foundation (ACI-0121475). Finally, we would like to thank early beta-testers of ELCIRC, who include CCALMR students Sergey Frolov, Michela Burla and Marina Vantrease; Dr. Mike Foreman (Institute of Ocean Sciences, Canada); and Drs. Anabela Oliveira and André Fortunato (Laboratório Nacional de Engenharia Civil, Portugal). SAR images (Figs. 1a, c) were purchased by Dr. Todd Sanders, under NOAA NESDIS Grant NA16EC2450.

Appendix A: Surface fluxes of heat and momentum

Atmospheric boundary conditions are required to model the exchange of heat and momentum between the atmosphere and the surface. We describe here the representation of exchanges adopted in ELCIRC when results from weather models are available as forcings. An alternative, more simplified, approach to representing momentum exchanges is described in the text (Section 2.3.1).

The total heat transfer across the air–water interface (into the water) is commonly described as

$$H_{tot}\downarrow = (1-A)R_s\downarrow + (R_{IR}\downarrow - R_{IR}\uparrow) - S - E, \tag{56}$$

where $H_{tot}\downarrow$ is the net downwards heat flux at the air–water interface, A is the albedo of the surface, $R_s\downarrow$ is the downwelling solar radiative flux at surface, $R_{IR}\downarrow$ and $R_{IR}\uparrow$ are the down/upwelling infrared radiative fluxes a the surface, S is the turbulent flux of sensible heat (upwelling), and E is the turbulent flux of latent heat (upwelling).

As stated in Section 2.3.3, the non-solar heat fluxes

$$H^*_{tot}\downarrow = (R_{IR}\downarrow - R_{IR}\uparrow) - S - E \quad at \quad z = H_R + \eta \tag{57}$$

are in ELCIRC applied as a surface boundary condition, Eq. (16), to the heat transport equation, Eq. (6). This is appropriate because both the infrared and turbulent fluxes essentially act at the surface of the water. Conversely, solar radiation is penetrative. The attenuation of solar radiation acts as a heat source within the water column, and is thus better expressed directly in Eq. (6), with

$$\dot{Q} = \frac{\partial R^*_s}{\partial z}. \tag{58}$$

The vertical profile of solar radiation is attenuated as in Paulson and Simpson (1977), given a predefined water type (Jerlov, 1968):

$$R^*_s(d_s) = (1-A)R_s\downarrow \left[\Re e^{-d_s/d_1} + (1-\Re)e^{-d_s/d_2}\right], \tag{59}$$

where d_s is the water depth (defined in Eq. (31)), and d_1, d_2, and $\Re$ are constants characterizing the turbidity of the chosen water type.

The downwelling radiative fluxes in Eqs. (57) and (58) are common output products of numerical weather prediction models, and the upwelling infrared radiation may be approximated as the blackbody radiative flux from the water's surface,

$$R_{IR}\uparrow = \in \sigma T_{sfc}^4, \tag{60}$$

where $\in$ is the emissivity (≈ 1), and σ is the Stefan–Boltzmann constant.

The turbulent fluxes of heat (S, E) and momentum (τ, Eq. (9)) are parameterized using the bulk aerodynamic formulation of Zeng et al. (1998). This parameterization has specifically been designed for improved accuracy in high-wind regimes, and takes into account surface layer stability, free convection, and variable roughness lengths:

$$S = -\rho_a c_{pa} u_* T_*, \quad E = -\rho_a L_e u_* q_*, \quad \tau = \rho_a u_*^2, \tag{61}$$

where T_*, u_*, and q_* are scaling parameters for air temperature, air velocity, and specific humidity; ρ_a is the surface air density, c_{pa} is the specific heat of air, and L_e is the latent heat of vaporization. The scaling parameters are defined using the dimensionless flux–gradient relations of Monin–Obukhov similarity theory, and must be solved for iteratively. They depend upon near-surface temperatures or water and air, wind speed, and specific humidity, as well as surface atmospheric pressure (all of which may also be obtained from numerical weather predictions).

References

Baptista, A.M., 1987. Solution of advection-dominated transport by Eulerian–Lagrangian methods using the backwards methods of characteristics. Civil Engineering. Cambridge, MA, USA, Ph.D. Thesis, Massachusetts Institute of Technology, 260pp.

Baptista, A.M., 2002. Environmental Observation and Forecasting Systems. In: Meyers, R.A. (Ed.), Encyclopedia of Physical Science and Technology, Vol. 5. Academic Press, New York, p. 16.

Baptista, A.M., Adams, E.E., Stolzenbach, K.D., 1984. Eulerian–Lagrangian analysis of Pollutant Transport in Shallow Water. MIT R. M. Parsons Laboratory, Cambridge, MA, USA.

Baptista, A. M., Wilkin, M., Pearson, P., Turner, P., McCandlish, C., Barrett, P., Das, S., Sommerfield, W., Qi, M., Nangia, N., Jay, D., Long, D., Pu, C., Hunt, J., Yang, Z., Myers, E., Darland, J., Farrenkopf, A., 1998. Towards a multi-purpose forecast system for the Columbia River Estuary. Ocean Community Conference '98, Baltimore, MD, USA.

Baptista, A.M., Wilkin, M., Pearson, P., Turner, C., McCandlish, C., Barrett, P., 1999. Coastal and estuarine forecast systems: a multi-pupose infrastructure for the Columbia River. Earth Sys. Mon./NOAA 9(3).

Baptista, A. M., Y. Zhang, A. Chawla, E. Myers, M. Zulauf, 2004. A cross-scale model for 3D baroclinic circulation in estuary–plume–shelf systems: II. Application to the Columbia River. Continental Shelf Research, in preparation.

Blumberg, A.F., Mellor, G.L., 1987. A description of a three-dimensional coastal ocean circulation model. In: Heaps, N. (Ed.), Three-Dimensional Coastal Ocean Models, Vol. 4. AGU, Washington, DC, USA, pp. 1–16.

Canuto, V.M., Howard, A., Cheng, Y., Dubovikov, M.S., 2001. Ocean turbulence I: one-point closure model. Momentum and heat vertical diffusivities. Journal of Physical Oceanography 31, 1413–1426.

Casulli, V., Cattani, E., 1994. Stability, accuracy and efficiency of a semi-implicit method for 3D shallow water flow. Computers & Mathematics with Applications 27, 99–112.

Casulli, V., Cheng, R.T., 1992. Semi-implicit finite difference methods for three-dimensional shallow water flow. International Journal of Numerical Methods in Fluids 15, 629–648.

Casulli, V., Zanolli, P., 1998. A three-dimensional semi-implicit algorithm for environmental flows on unstructured grids. Institute for Computational Fluid Dynamics Conference on Numerical Methods for Fluid Dynamics VI.

CCALMR, 2003. ELCIRC. WWW Page. http://www.ccalmr.ogi.edu/CORIE/modeling/elcirc, Center for Coastal and Land-Margin Research (CCALMR), Oregon Health & Science University, OR, USA.

Flather, R.A., 1987. A tidal model of Northeast Pacific. Atmosphere–ocean 25 (1), 22–45.

Foreman, M.G.G., Henry, R.F., Walters, R.A., Ballantyne, V.A., 1993. A finite element model for tides and resonance along the north coast of British Columbia. Journal of Geophysical. Research 98 (C2), 2509–2531.

Galperin, B., Kantha, L.H., Hassid, S., Rosati, A., 1988. A quasi-equilibrium turbulent energy model for geophysical flows. Journal of Atmospheric Science 45, 55–62.

Garcia-Berdeal, I., Hickey, B.M., Kawase, M., 2002. Influence of wind stress and ambient flow on a high discharge river plume. Journal of Geophysical. Research 107 (C9), 3130.

Haidvogel, D.B., Arango, H.G., Hedstrom, K., Beckmann, A., Malanotte-Rizzoli, P., Shchepetkin, A.F., 2000. Model evaluation experiments in the North Atlantic Basin: simulations in nonlinear terrain-following coordinates. Dynamics of Atmosphers and Oceans 32, 239–281.

Iskandarani, M., Haidvogel, D.B., Levin, J., 2003. A three-dimensional spectral element model for the solution of the hydrostatic primitive equations. Journal of Computational Physics 186 (2), 397–425.

Jerlov, N.G., 1968. Optical Oceanography. Elsevier, Amsterdam.

Kantha, L.H., Clayson, C.A., 1994. An improved mixed layer model for geophysical applications. Journal of Geophyscial Research 99 (25), 235–266.

Lehfeldt, R., Bloss, S., 1988. Algebraic turbulence model for stratified tidal flows. In: Dronkers, J., Leussen, W.v. (Eds.), Physical processes in estuaries. Springer, New York.

Luettich, R.A., Westerink, J.J., Scheffner, N. W., 1991. ADCIRC: an advanced three-dimensional circulation model for shelves, coasts and estuaries, Coast. Engrg. Res. Ct., US Army Engs. Wtrways. Experiment Station, Vicksburg, MS.

Luettich, R.A., Muccino, J.C., Foreman, M.G.G., 2002. Considerations in the calculation of vertical velocity in three-dimensional circulation models. Journal of Atmospheric and Oceanic Technology 19 (12), 2063–2076.

Lynch, D.R., Gray, W.G., 1978. Analytic solutions for computer flow model testing. ASCE Journal of the Hydraulics Division 104 (HY10), 1409–1428.

Lynch, D.R., Ip, J.T., Naimie, C.E., Werner, F.E., 1996. Comprehensive coastal circulation model with application to the Gulf of Maine. Continental Shelf Research 16 (7), 875–906.

Mellor, G.L., Yamada, T., 1982. Development of a turbulence closure model for geophysical fluid problems. Reviews in Geophys 20, 851–875.

Millero, F.J., Poisson, A., 1981. International one-atmosphere equation of state of sea-water. Deep-Sea Research 28A, 625–629.

Munk, W.H., Anderson, E.R., 1948. Notes on a theory of the thermocline. Journal of Marine Research 7, 276–295.

Myers, E., Aikman, F., 2003. A forecast circulation model of the St. Johns River, Florida. 8th Estuarine and Coastal Modeling Conference, Monterey Bay, CA, USA.

Oey, L.Y., Mellor, G.L., 1993. Subtidal variability of estuarine outflow, plume, and coastal current: a model study. Journal of Physical Oceanography 23, 164–176.

Oliveira, A., Baptista, A.M., 1995. A comparison of integration and interpolation Eulerian-Lagrangian methods. International Journal of Numerical Methods in Fluids 21, 183–204.

Oliveira, A., Baptista, A.M., 1998. On the role of tracking on Eulerian-Lagrangian solutions of the transport equation. Advances in Water Resources 21, 539–554.

Oliveira, A., Fortunato, A., Baptista, A.M., 2000. Mass Balance in Eulerian-Lagrangian Transport Simulations in Estuaries. ASCE Journal of Hydraulic Engineering 126 (8), 605–614.

Pacanowski, R.C., Philander, S.G.H., 1981. Parameterization of vertical mixing in numerical models of tropical oceans. Journal of Physical Oceanography 11, 1443–1451.

Paulson, C.A., Simpson, J.J., 1977. Irradiance measurements in the upper ocean. Journal of Physical Oceanography 7, 952–956.

Pinto, L.L., Oliveira, A., Fortunato, A. B., Baptista, A. M., 2003. Analysis of the stratification in the Guadiana estuary. 8th Estuarine and Coastal Modeling Conference, Monterey Bay, CA.

Pond, S., Pickard, G.L., 1998. Introductory Dynamical Oceanography. Butterworth-Heinmann, Stoneham, MA.

Reid, R.O., 1990. Waterlevel changes. Handbook of Coastal and Ocean Engineering. Gulf Publishing, Houston, Tx.

Robinson, C.L.K., Morrison, J., Foreman, M.G.G., 2004. Oceanographic connectivity among marine protected areas on Canada's northern Pacific coast. Marine Ecology Progress Series (submitted).

Rodi, W., 1984. Turbulence models and their applications in hydraulics: a state of the art review. Delft, The Netherlands, International Association for Hydraulics Research.

Song, Y., Haidvogel, D., 1994. A semi-implicit ocean circulation model using a generalized topography-following coordinate system. Journal of Computatinal Physics 115, 228–244.

Turner, P.J., Baptista, A.M., 1991. User's manual: software for semi-automatic generation of two-dimensional finite element grids, OGI-CCALMR Software Documentation Series SDS2–91/2.

Umlauf, L., Burchard, H., 2003. A generic length-scale equation for geophysical turbulence models. Journal of Marine Research 6 (12), 235–265.

Vaz, R.A., Simpson, J.H., 1994. Turbulence closure modeling of estuarine stratification. Journal of Geophysical Research 99 (C8), 16143–16160.

Wang, D.-P., 1984. Mutual intrusion of a gravity current and density front formation. Journal of Physical Oceanogr 14, 1191–1199.

Warner, J.C., Sherwood, C.R., Arango, H.G., Signell, R.P., 2004. Performance of four turbulence closure models implemented using a generic length scale method. Ocean Modeling (in press).

Wilcox, D.C., 1998. Reassessment of scale determining equation for advance turbulence models. AIAA Journal 26, 1299–1310.

Wood, T.M., Baptista, A.M., Kuwabara, J.S., Flegal, A.R., 1995. Diagnostic modeling of trace metal partitioning in south San Francisco Bay. Limnology in Oceanography 40 (2), 345–358.

Zeng, X., Zhao, M., Dickinson, R.E., 1998. Intercomparison of bulk aerodynamic algorithms for the computation of sea surface fluxes using TOGA COARE and TAO data. Journal of Climatology 11, 2628–2644.

Zhang, Y., Baptista, A.M., 2000. An efficient adaptive editor for unstructured grids. 7th International Conference on Numerical Grid Generation in Computational Field Simulations, Whistler, BC, Canada.